

Impact of Toxoplasma ROPs/GRAs on Host Transcription

1 **Differential Impacts on Host Transcription by ROP and GRA Effectors from the** 2 **Intracellular Parasite *Toxoplasma gondii***

3 Suchita Rastogi¹, Yuan Xue², Stephen R. Quake^{*,2,3,4,#}, John C. Boothroyd^{*,2,#}

4 *Equal contribution

5

6 ¹Department of Microbiology and Immunology, Stanford University School of Medicine, Stanford,
7 CA, USA

8 ²Department of Bioengineering, Stanford University, Stanford, CA, USA

9 ³Department of Applied Physics, Stanford University, Stanford, CA, USA

10 ⁴Chan Zuckerberg Biohub, San Francisco, CA, USA

11

12 #Correspondence should be addressed to J.C.B. (jboothr@stanford.edu) and S.R.Q.

13 (steve@quake-lab.org).

14

15

16 Abstract: 220 words

17 Importance: 36 words

18 Text: 8,289 words

19

20

21

22

23

24 **Differential Impacts on Host Transcription by ROP and GRA Effectors from the**
25 **Intracellular Parasite *Toxoplasma gondii***

26 Suchita Rastogi, Yuan Xue, Stephen R. Quake*, John C. Boothroyd*

27

28 * Equal contribution

29

30 **ABSTRACT**

31 The intracellular parasite *Toxoplasma gondii* employs a vast array of effector
32 proteins from the rhoptry and dense granule organelles to modulate host cell biology;
33 these effectors are known as ROPs and GRAs, respectively. To examine the individual
34 impacts of ROPs and GRAs on host gene expression, we developed a robust, novel
35 protocol to enrich for ultra-pure populations of a naturally occurring and reproducible
36 population of host cells called uninfected-injected (U-I) cells, which *Toxoplasma* injects
37 with ROPs but subsequently fails to invade. We then performed single cell
38 transcriptomic analysis at 1-3 hours post-infection on U-I cells (as well as on uninfected
39 and infected controls) arising from infection with either wild type parasites or parasites
40 lacking the MYR1 protein, which is required for soluble GRAs to cross the
41 parasitophorous vacuole membrane (PVM) and reach the host cell cytosol. Based on
42 comparisons of infected and U-I cells, the host's earliest response to infection appears
43 to be driven primarily by the injected ROPs, which appear to induce immune and
44 cellular stress pathways. These ROP-dependent pro-inflammatory signatures appear to
45 be counteracted by at least some of the MYR1-dependent GRAs and may be enhanced
46 by the MYR-independent GRAs, (which are found embedded within the PVM). Finally,

47 signatures detected in uninfected bystander cells from the infected monolayers
48 suggests that MYR1-dependent paracrine effects also counteract inflammatory ROP-
49 dependent processes.

50

51 **IMPORTANCE**

52 This work performs the first transcriptomic analysis of U-I cells, captures the
53 earliest stage of a host cell's interaction with *Toxoplasma gondii*, and dissects the
54 effects of individual classes of parasite effectors on host cell biology.

55

56 **MAIN TEXT**

57 **Introduction**

58 The obligate intracellular parasite *Toxoplasma gondii* parasitizes a wide range of
59 avian and mammalian organisms, including humans (1). During the acute phase of
60 infection, this unicellular eukaryote rapidly expands within host tissues by penetrating
61 host cells, establishing and replicating within an intracellular parasitophorous vacuole
62 (PV), and simultaneously avoiding clearance by the host immune system (reviewed in
63 (2)). To orchestrate these events, *Toxoplasma* employs a vast repertoire of effector
64 proteins housed primarily in two secretory organelles, the rhoptries and dense granules
65 (Fig. 1A). The rhoptry organelle effectors (ROPs) are secreted by the parasite into the
66 host cytosol during or immediately prior to invasion by an as yet undefined mechanism
67 (reviewed in (3)). The handful of ROPs that have been characterized to date include
68 virulence factors that disrupt immune clearance mechanisms (4-7), remodel the host's
69 cortical actin cytoskeleton at the point of parasite penetration (8, 9), and co-opt the

70 STAT3 and STAT6 pathways (10-12). In contrast, the dense granule effectors (GRAs)
71 are thought to be secreted later during the invasion process and mostly after the
72 parasite has invaded the host cell (reviewed in (3)). Many GRAs remain in the PV lumen
73 or PV membrane (PVM) (13-17), but others traverse the PVM to reach the host cytosol
74 and often proceed to the host nucleus (18-24). The translocation of this latter class of
75 GRAs across the PVM is dependent on a group of PVM proteins called the MYR
76 complex, i.e., MYR1, MYR2, and MYR3, which are so-named because they are
77 required for parasite-dependent host c-Myc regulation (25-27). Host signaling pathways
78 modulated by the PVM-embedded, MYR-independent GRAs (MIGs) include the nuclear
79 factor kappa light chain enhancer of activated B cells pathway. Host pathways
80 modulated by MYR-dependent GRAs (MDGs) include the interferon gamma (IFN-
81 gamma), mitogen activated protein kinase, and p53 pathways, as well as the cyclin E
82 regulatory complex (22, 23, 28).

83 The collective host response to ROPs, MDGs, MIGs, and other perturbations
84 during infection with *Toxoplasma gondii* have been well-documented in transcriptomic
85 studies that compare infected and mock-infected cells; however, the contribution of
86 individual parasite effector compartments to the overall picture is more poorly defined,
87 particularly because many parasite effectors are introduced during the earliest stages of
88 infection in very narrow time intervals. Specifically, invasion is a rapid process that takes
89 approximately 40 seconds (29), and deployment of the ROPs likely occurs during the
90 first third of invasion in one shot (30). In contrast, MDGs have been detected by
91 immunofluorescence assays in the nuclei of parasitized host cells at ~3 hours post-
92 invasion at the earliest (19), which suggests that they likely modulate host transcription

93 much later than ROPs. Parasite mutants that lack a functional MYR complex have
94 helped separate the impact of MDGs from those of other parasite effectors (25, 26, 31),
95 but the specific impact on host transcription by ROPs and MIGs has yet to be
96 determined. The rhoptry organelle's contribution is of particular interest given that ROP
97 injection is essential to parasite invasion, survival, and virulence, and that the functions
98 of most ROPs are unknown.

99 Here we document the impact of specific classes of parasite effectors, including
100 for the first time ROPs, by leveraging a rare population of host cells that parasites inject
101 with ROPs but subsequently fail to invade (32). These uninfected-injected (U-I) host
102 cells (Fig. 1B) do not arise as a result of parasite-derived exosomes delivering effectors
103 to host cells (32) or due to impending host cell death (Fig. 2B). They arise
104 spontaneously in tissue culture during *Toxoplasma* infection and may also arise *in vivo*
105 in the brains of mice chronically infected with *Toxoplasma* (32). To interrogate the host
106 response specifically to effectors injected before invasion, we developed a novel
107 pipeline to purify and perform single cell RNA sequencing (scRNA-seq) of U-I cells, as
108 well as of infected and uninfected controls from the same host cell monolayer. To
109 resolve the impact of effectors released during vs. after invasion, we also analyzed U-I
110 cells, infected cells, and uninfected cells from host cell monolayers infected with
111 parasites lacking MYR1, a component of the complex required for translocation of
112 MDGs into the host cytosol (25, 26). Our findings reveal new insight into the impact of
113 individual parasite effector compartments on the biology of *Toxoplasma*-infected host
114 cells.

115

116 **Results**

117 ***A Novel FACS-Based Single Cell RNA Sequencing Pipeline Captures***

118 ***Transcriptomic Signatures of Individual Effector Compartments***

119 According to the current model of parasite effector secretion (Fig. 1A), the host
120 response to an infection with *Toxoplasma* tachyzoites can be attributed to 5 parasite-
121 dependent stimuli: 1) the secretion of paracrine effectors into the extracellular milieu; 2)
122 injection of ROPs; 3) activity of MIGs; 4) secretion of MDGs; and 5) parasite invasion
123 and establishment of the PV. To resolve the individual impacts of each of these classes
124 of stimulus, we transcriptomically profiled infected, uninfected, and U-I host cells from
125 monolayers exposed to parasites. To this end, we devised a novel pipeline in which: 1)
126 infections were designed to generate a heterogeneous pool of host cells each impinged
127 upon by one of several combinations of parasite-dependent stimuli; 2) a fluorescence
128 activated cell sorting (FACS)-based protocol was employed to separate host cells of
129 interest from infected monolayers based on the parasite-dependent stimuli by which
130 they were affected; and 3) the host cell transcriptomes were profiled by full-length
131 scRNA-seq. Given the novelty and complexity of this pipeline, before we delineate our
132 biological findings, here we present an account of our strategy and technical findings
133 during pipeline development.

134

135 ***FACS-Based Isolation of Host Cells for Single Cell RNA Sequencing Purifies***

136 ***Uninfected-Injected Cells***

137 To generate host cells impacted by various combinations of parasite-dependent
138 stimuli for downstream RNA-seq, we subjected the host cells to infection with either wild

139 type RH (type I) strain parasites, mutant $\Delta myr1$ parasites lacking the MYR1 protein
140 (constructed from an RH $\Delta myr1$ mCherry parental strain (25); Fig. S1)), or a parasite-
141 free cell lysate (i.e., mock infection) from the feeder human foreskin fibroblast (HFF)
142 cells used to maintain both parasite lines. From here on, we designate host cells that
143 arose from the wild type, $\Delta myr1$, and mock infections as Wt, Dmyr1, or Mock cells,
144 respectively. All parasites were engineered to express the ROP fusion protein toxofilin-
145 beta-lactamase (Tfn-BLA) as well as a constitutive red fluorescent protein. In addition,
146 we chose 10 T1/2 mouse fibroblasts as the preferred host cell type over conventionally
147 used HFFs, which we found unsuitable for single cell sorts due to their propensity to
148 remain clumped in FACS buffer.

149 As each true infection results in a heterogeneous monolayer containing U-I cells,
150 infected cells (designated I-I for being infected and injected), and uninfected cells
151 (denoted U-U for being uninfected and uninjected; Fig. 1B), the infection conditions
152 yielded seven key species of host cell: Wt U-I, Wt I-I, Wt U-U, Dmyr1 U-I, Dmyr1 I-I,
153 Dmyr1 U-U, and Mock. Each of these species was expected to be influenced by a
154 specific combination of parasite-dependent stimuli (Fig. 1C). By comparing the
155 transcriptomes of key pairs of these seven cell species (see Materials and Methods,
156 Data Availability), we expected to uncover the impact of previously unexamined
157 parasite-dependent stimuli, e.g., ROPs (summarized in Fig. 1D). Of note, these
158 experimental conditions enabled transcriptomic assessment of paracrine effects during
159 *Toxoplasma* infection (by comparison of U-U vs. mock-infected cells) and generated
160 pure I-I and U-I cell populations at extremely short infection durations, an improvement

161 over traditional methods that rely on high multiplicities of infection and long infection
162 times to distinguish infected vs. uninfected transcriptomic signatures.

163 To capture individual cells from each cell species, we devised a FACS-based
164 protocol that purified each species from the host cell monolayers (Fig. 2A). The pipeline
165 employed the toxofilin-beta-lactamase (Tfn-BLA) assay (8), in which the (mock)-infected
166 host cell monolayers were stained for 30 minutes with CCF2-AM, a reporter dye that is
167 taken up by live host cells and shifts from green to blue fluorescence when cleaved by
168 beta-lactamase. CCF2-AM staining occurred at 30, 90, or 150 minutes post-infection, to
169 yield cells at 1, 2, or 3 hours post-infection (hpi). In addition, CCF2-AM staining was
170 performed at room temperature (23 °C) to preserve the integrity of the CCF2-AM dye,
171 which decomposes at 37 °C. U-I cells were then FACS sorted based on their blue
172 (cleaved) CCF2-AM fluorescence and their absent red fluorescence (since they lacked
173 internalized parasites). In addition, I-I cells were sorted for their double positive blue
174 (from cleaved CCF2-AM) and red (from internalized parasites) fluorescence, and U-U
175 and Mock cells were sorted for their green (cleaved) CCF2-AM fluorescence. Single
176 cells and bulk populations of 50-100 cells of each cell species were collected.

177 To ensure confidence in the identity of the sorted cells and to limit the number of
178 parasites per I-I cell to one, we gated stringently during FACS, particularly for the “U-I
179 cells” gate and “parasite-associated” gate (which included I-I cells; Fig. 2B). We also
180 subjected all cells to extensive washes before FACS sorting, as debris from the human
181 feeder cells used to culture the parasites contaminates the U-I gate (Fig. S2), likely due
182 to retention of both CCF2-AM dye and the parasite fusion protein Tfn-BLA. Of note, the
183 debris posed significant challenges to downstream bioinformatic analyses of bulk U-I

184 cells, but they registered as single cells in the scRNA-seq pipeline and were
185 automatically discarded during quality control due to their high percentage of human
186 reads. At a multiplicity of infection of ~ 6 , U-I cells constituted $\sim 8.8\%$ of the injected (i.e.,
187 U-I + I-I) cell population at 1 hpi, $\sim 2.0\%$ at 2 hpi, and $\sim 3.4\%$ at 3 hpi (Fig. 2C).
188 Abundances of sorted U-I, I-I, and U-U cells relative to all sorted cells are depicted in
189 Fig. 2D.

190 To validate U-I cells as appropriate models for host responses to injected
191 parasite effectors, we also limited the possibility of U-I cells arising by mechanisms
192 other than aborted invasion events. One such mechanism is host immune clearance of
193 internalized parasites. However, this route is an unlikely source of U-I cells in our
194 pipeline for two reasons: 1) immune clearance of intracellular pathogens in mouse cells
195 is activated by exogenous IFN-gamma, which we did not add to the host cells, and 2) all
196 known strains of *Toxoplasma* escape IFN-gamma-mediated pathogen clearance by
197 suppressing the IFN-gamma signaling pathway if they infect the host cell before it is
198 exposed to extracellular IFN-gamma (33, 34). In another potential mechanism, an
199 infected host cell may divide and produce an uninfected daughter (a U-I_d cell, for U-I by
200 division). To limit the occurrence of U-I_d cells, we serum starved all host cells for the 24
201 hours preceding infection to induce cell cycle arrest (Fig. S3A) and limited infection
202 durations to 3 hpi or less, as live video microscopy of 200 parasite-infected, serum-
203 starved 10 T1/2 host cells for 16 hours revealed that no infected cell divided before 3.67
204 hpi (Fig. S3B). Finally, a newly internalized parasite might spontaneously exit early from
205 the host cell, a rare and poorly characterized process that is therefore difficult to control.
206 Though we cannot exclude the possibility that a very small number of our U-I cells arose

207 from this mechanism of premature parasite egress, and though U-I_d production cannot
208 be completely ruled out, an advantage of scRNA-seq is its ability to distinguish
209 differences between cells arising via different mechanisms (assuming they differ
210 transcriptomically).

211

212 *Technical Validation of Single Cell Sequencing for Cells Exposed to or Parasitized by*
213 *Toxoplasma gondii*

214 Given the limited duration of infection (≤ 3 hours), we expected relatively subtle
215 transcriptional changes in U-I and I-I cells. To maximize the sensitivity of scRNA-seq
216 analyses to detect such signatures, we employed Smart-seq2 library preparation and
217 sequenced to a depth of 1 million reads per cell. All reads were aligned to a
218 concatenated mouse-*Toxoplasma* genome using the genomic sequence for the GT1
219 parasite strain, a clonal relative of RH (35, 36). In addition, we identified and discarded
220 43 mouse genes to which reads from extracellular RH parasites aligned (mostly
221 representing evolutionarily conserved genes; Table S1).

222 To ensure that poorly amplified or poorly sequenced host cells did not confound
223 downstream analysis, we filtered samples based on several quality metrics (Materials
224 and Methods), yielding 453, 2,026, and 2,875 cells at 1, 2, and 3 hpi, respectively, for
225 downstream analysis (Fig. S4A). Mapping efficiency of the analyzed cells was >85% in
226 all experimental trials (Fig. S4B). Characterization of measurement sensitivity based on
227 logistic regression modeling of ERCC spike-in standards revealed a 50% detection rate
228 of 31, 11, and 34 RNA molecules per cell at 1 hpi, 2 hpi, and 3 hpi, respectively (Fig.
229 S4C), amounting to a level of sensitivity comparable to that previously reported (37).

230 After filtering out genes with expression above the detection limit in <6 cells, we
231 normalized for sequencing depth across cells by dividing each read count by the
232 median read sum to yield counts in units of counts per median (cpm) (Materials and
233 Methods). Gene expression in the scRNA-seq dataset exhibited a strong positive
234 correlation to expression in bulk RNA-seq samples processed the same way specifically
235 for differentially expressed genes (DEGs) between experimental conditions (i.e., U-U, I-I,
236 and U-I cells; Fig. S4D). Furthermore, each bulk experiment's expression data exhibited
237 the best correlation with their cognate single cell data (Fig. S4E). Taken together, these
238 data demonstrate that scRNA-seq captures similar transcriptomic signatures in host
239 cells to those detected in bulk RNA-seq experiments, validating the scRNA-seq platform
240 as an approach to further characterize host cell transcriptomic responses during
241 *Toxoplasma* infection.

242

243 Single Cell Resolution Reveals Cell-to-Cell Heterogeneity Inaccessible to the Bulk RNA

244 Sequencing Platform

245 A key advantage of single cell resolution is that it enables identification and
246 separation of parasite-independent host cell heterogeneity. Accordingly, single cell
247 resolution facilitates an extra checkpoint to validate the identities of U-I, I-I and U-U cells
248 by quantifying the percentage of *Toxoplasma*-derived reads in each cell. As expected,
249 *Toxoplasma* read content across all cells exhibited a bimodal distribution, where most
250 uninfected cells contained <0.01% *Toxoplasma* reads, while most infected cells
251 possessed higher percentages, i.e., 0.5-4%. However, a small proportion of U-I cells
252 and I-I cells exhibited unexpectedly high (for U-I) or low (for I-I) *Toxoplasma* read counts

253 and were considered to be misclassified (Fig. S5A). This may have resulted from a low
254 rate of TdTomato or mCherry loss in some of the parasites (for cells misclassified as U-I)
255 or from attached but not fully invaded parasites being dislodged from the host cell at
256 some point between fluorescence detection and deposition of the cell into lysis buffer
257 (for cells misclassified as I-I). Such misclassified cells may have contributed significant
258 and potentially misleading signatures to their respective samples. To preclude this
259 possibility in our single cell dataset, we excluded all U-I cells with >0.04% *Toxoplasma*
260 reads and all I-I cells with <0.32% *Toxoplasma* reads from downstream analysis.

261 Next, because the experimental pipeline examined cells during their earliest
262 interaction with *Toxoplasma*, we expected the subtle, parasite-dependent transcriptional
263 signatures to be potentially eclipsed by intrinsic host processes such as cell cycle,
264 which still progressed in some cells even with serum starvation (Fig. S3A). To separate
265 host cell cycle from other biological processes the parasites could potentially modulate,
266 we determined the phases of all single cells (i.e., G1, S, or G2/M) based on expression
267 of 175 curated cell cycle marker genes (Fig. S5B; Table S2; Materials and Methods). A
268 breakdown of cell cycle phase composition for each experimental condition across all
269 time points revealed a consistent pattern at 2 hpi in which the proportion of cells in G2
270 or M phase increased in a manner that appeared dependent on injected effectors, i.e.,
271 from 13.3% in Mock to 33.9% in Wt U-I, 41.4% in Dmyr1 U-I, and 22.5% in CytD U-I; Fig.
272 S5C). These findings are consistent with potential induction of cell cycle arrest in U-I
273 cells by injected effectors, as previously reported (38-41).

274 To identify other sources of heterogeneity in the dataset, we used the *Uniform*
275 *Manifold Approximation and Projection* (UMAP) algorithm for dimensionality reduction

276 and to visualize relationships between all cells based on the most dispersed (i.e.,
277 variable) genes. Leiden clustering revealed three distinct clusters, designated herein as
278 populations 1, 2, and 3 (Fig. S5D). Curiously, cells from different time points exhibited
279 differences in the proportion of cells belonging to each population, where 2 hpi cells fell
280 entirely in population 1, and 3 hpi cells fell in all three populations. In conventional single
281 cell analysis, dimensionality reduction and cell clustering are used to identify novel cell
282 types. Though the 10 T1/2 host cell line used in our experiments is clonal, it is derived
283 from a pluripotent stem cell population that has a propensity to differentiate, such that
284 the three identified populations could conceivably represent distinct differentiation states
285 (42).

286 To limit cell-to-cell heterogeneity from overshadowing potentially subtle
287 transcriptomic signatures induced by parasite effector secretion and parasite invasion,
288 we limited our remaining analyses to host cells in G1 phase (to limit cell cycle
289 signatures) and from UMAP population 1 (to factor out potential cell type signatures).

290

291 ***Injected Parasite Effectors Drive Inflammatory Transcriptional Signatures***

292 ***Associated with Parasite Infection***

293 Having established a robust pipeline to isolate, RNA sequence, and
294 bioinformatically analyze the transcriptomes of individual cells from each of seven
295 relevant cell species (i.e., Wt U-I, Wt I-I, Wt U-U, Dmyr1 U-I, Dmyr1 I-I, Dmyr1 U-U, and
296 Mock cells; Fig. 1C), we next sought to determine host responses to each of five
297 individual classes of parasite-dependent stimuli, namely rhoptry proteins (ROPs), MYR-
298 dependent dense granule proteins (MDGs), MYR-independent dense granule proteins

299 (MIGs), parasite invasion, and paracrine effects. To isolate each parasite-dependent
300 stimulus, we used the Model-based Analysis of Single Cell Transcriptomics (MAST)
301 algorithm to perform differential gene expression analysis on key pairs of the seven
302 relevant cell species from the pool of G1 phase, UMAP population 1 cells. Across all
303 pairwise comparisons between conditions within each time point, 39, 2,252, and 10,995
304 differentially expressed genes (DEGs) were detected at 1 hpi, 2 hpi, and 3 hpi,
305 respectively (Table S3A). These results show that parasite effectors and invasion result
306 in almost no detectable transcriptional response at 1 hpi, a modest response involving
307 regulation of a core group of genes at 2 hpi, and ramping up of this response at 3 hpi in
308 which transcription in a much larger set of host cells is modulated. Because of the
309 negligible response at 1 hpi, we excluded data from this time point from the remaining
310 analyses.

311 For additional validation, we assessed the 2 hpi and 3 hpi datasets for their
312 agreement with two previous bulk RNA-seq studies that captured the host response to
313 infection at 6 hpi in nominally the same parasite strains and culture conditions, albeit in
314 HFFs instead of mouse 10 T1/2 fibroblasts (10, 31). Because these studies measured
315 the infection response by comparing infected vs. mock-infected cells, we examined
316 DEGs between Wt I-I and mock-infected (i.e., Mock) cells in our own datasets. Gene set
317 enrichment analysis (GSEA) of the resulting DEGs at 2 hpi and 3 hpi (Table S3B) using
318 the Molecular Signatures Database's Hallmark gene sets (43) revealed that nearly all
319 significantly enriched gene sets at 2 hpi and 3 hpi were previously identified in the Naor
320 et al. reference dataset, and many pertained to immune processes (Fig. 3; 31). Of note,
321 gene sets were considered to be significantly enriched if their false discovery rates were

322 < 0.25, a standard cutoff for GSEA given the lack of coherence in most transcriptional
323 datasets and the relatively low number of gene sets being analyzed. Nearly all gene
324 sets *not* preserved in the Naor et al. reference were enriched from genes
325 *down*regulated upon infection. The lack of agreement between our downregulated gene
326 sets and those obtained from the references likely reflects the infection response's
327 tendency towards gene *up*regulation, and to stochasticity in expression levels for the
328 substantially fewer downregulated genes detected, an interpretation corroborated by the
329 downregulated genes' higher p-values and lower fold changes. Overall these results
330 indicate that the 2 hpi and 3 hpi datasets capture well-known host responses to infection
331 with *Toxoplasma gondii*.

332 Next, to determine the host response to injection of parasite effectors, we
333 compared U-I cells from wild type parasite infection (i.e., Wt U-I cells) to uninfected cells
334 from the same monolayer (i.e., Wt U-U cells). At 2 hpi, only 10 DEGs were identified
335 (Table S3C), and GSEA of these DEGs revealed no significant enrichment of the
336 Hallmark gene sets. Therefore, injection of parasite effectors without invasion appears
337 to elicit only a trace response at 2 hpi. At 3 hpi, 156 DEGs were detected between Wt
338 U-I and Wt U-U cells (Table S3C), for which GSEA revealed a total of 17 gene sets (Fig.
339 4A); 14 corresponded to genes expressed higher in Wt U-I cells than in Wt U-U cells,
340 and several were associated with inflammation. In addition, 10 gene sets were common
341 to the infection response, i.e., also enriched in Wt I-I vs. Mock DEGs (Fig. 3), which
342 suggests that much of the early response to parasite infection is driven by the injection
343 of parasite effectors (likely ROPs) into host cells prior to invasion.

344 To confirm that the transcriptional signatures in Wt U-I cells originated from ROP
345 injection, we made two additional comparisons. For the first, we compared U-I cells
346 from $\Delta myr1$ parasite infection (i.e., Dmyr1 U-I cells) to uninfected cells from the same
347 monolayer (i.e., Dmyr1 U-U cells). As MDGs fail to traverse the PVM during $\Delta myr1$
348 parasite infections, the absence of MYR1 should effectively limit the parasites' effector
349 repertoire to ROPs and MIGs; consequently, transcriptional signatures from Dmyr1 U-I
350 cells and Wt U-I cells should largely resemble one another. In the second comparison,
351 to account for the possibility that Wt U-I signatures originated from a pre-existing
352 difference in those host cells from their neighbors, rather than from injected effectors,
353 we collected U-U, U-I, and I-I cells from host monolayers exposed to wild type parasites
354 pre-treated with the invasion inhibitor cytochalasin D, which allows parasite attachment
355 but blocks subsequent invasion. As expected, cytochalasin D treatment increased the
356 proportion of U-I cells in infected monolayers by ~6-fold at 2 hpi and by ~9.3-fold at 3
357 hpi (Fig. S6), so at least 85-90% of the artificially induced U-I cells (i.e., CytD U-I cells)
358 presumably arose from drug-induced abortion of parasite invasion events, rather than
359 from parasite-independent host cell differences. We predicted that transcriptional
360 signatures detected in CytD U-I cells would be driven almost entirely by injected
361 parasite effectors and would mirror those identified in both Wt U-I and Dmyr1 U-I cells.

362 As expected, at 2 hpi very few DEGs (29 and 51, respectively) and no enriched
363 gene sets were identified for Dmyr1 and CytD U-I cells vs. their corresponding U-U cells,
364 while at 3 hpi substantially more DEGs (103 and 174 for Dmyr1 and CytD U-I vs. U-U
365 cells, respectively) and gene sets were identified (Table S3D; Table S3E). The 3 hpi
366 gene sets exhibited a strong degree of overlap with the original Wt U-I vs. Wt U-U

367 comparison, such that 14 of the 17 Wt U-I vs. Wt U-U gene sets were also identified in
368 one or both of the corresponding Dmyr1 and CytD comparisons (Fig. 4B). These data
369 are consistent with an inflammatory response to ROP injection that drives much of the
370 host cell's total response to parasite infection.

371 In light of the many shared genes and gene sets between the infection vs.
372 injection responses, we next sought to define the distinction between these responses
373 by comparing Wt U-I (injected) to Wt I-I (infected) cells using two complementary
374 approaches. In the first approach, we used MAST to identify DEGs between Wt U-I and
375 Wt I-I cells and subjected the DEGs to GSEA. To better compare the trajectories of Wt
376 I-I and Wt U-I gene expression, we also computed fold changes in DEG expression
377 between each of these conditions and Wt U-U cells (Table S3F). In the second
378 approach, we identified genes with significant differences between Wt U-I and Wt I-I
379 cells in their correlation to a quantity called the CCF2-AM ratio, i.e., the ratio of blue
380 (cleaved) to green (uncleaved) CCF2-AM indicator dye detected during FACS sorting.

381 In this second approach, the CCF2-AM ratio was used as a quantitative proxy for
382 the influence of parasite-dependent effectors on individual host cells. Briefly, in the
383 strictest sense, the CCF2-AM ratio is a biological readout for penetration of a given host
384 cell by the injected ROP fusion protein Tfn-BLA, as the intracellular CCF2-AM dye in our
385 pipeline is cleaved by the beta-lactamase in Tfn-BLA. Since the host cells should exhibit
386 more or less equal loading of the CCF2-AM substrate, we presumed that the extent of
387 conversion in CCF2-AM signal from green (uncleaved) to blue (cleaved) reflected both
388 the concentration of Tfn-BLA protein introduced into the cell and the amount of time it
389 had spent within the cell. In Wt U-I cells, Tfn-BLA penetration occurs concomitantly with

390 injection of the other ROP effectors; therefore, the CCF2-AM ratio can be interpreted as
391 a quantitative measure for ROP penetration in Wt U-I cells. Wt I-I cells, however, are
392 presumably penetrated not only by ROPs but also by MIGs, MDGs, and the parasites
393 themselves. Accordingly, since the amount of ROPs injected into cells and the time
394 ROPs spend inside cells likely track with the same quantities for the remaining parasite-
395 dependent stimuli, we used the CCF2-AM ratio in Wt I-I cells as a proxy for the
396 presence of all four parasite stimuli inside each cell. Next, we computed the Spearman
397 correlation between each gene's expression and the CCF2-AM ratio separately in both
398 Wt U-I cells and Wt I-I cells. Of note, because we calculated the correlation by
399 incorporating the CCF2-AM ratios from Wt U-U cells (which should be devoid of ROPs,
400 MIGs, MDGs, and parasites) as negative controls for both the Wt U-I and Wt I-I
401 analyses, the correlation data do not encapsulate the influence of parasite-dependent
402 stimuli that Wt U-U cells have in common with Wt U-I and Wt I-I cells, i.e., paracrine
403 factors. Finally, we identified genes that exhibited significant shifts between Wt U-I and
404 Wt I-I cells in their relationship to the CCF2-AM ratio (Table S4A) by first modeling a
405 Gaussian distribution of their Spearman correlations to the CCF2-AM ratio (Fig. 5A).
406 Genes that significantly deviated from the Gaussian distribution and that also exhibited
407 a sufficient difference in their CCF2-AM correlation scores in Wt U-I vs. Wt I-I cells were
408 interpreted to be associated with either ROP injection alone (in Wt U-I cells) or with all
409 secreted effectors plus parasites (in Wt I-I cells, in which ROP penetration should be
410 accompanied by all other parasite-induced insults).

411 Analysis of Wt I-I vs. Wt U-I cells at 2 hpi revealed no significant DEGs, pointing
412 to a profound similarity in host transcription in Wt I-I and Wt U-I cells at 2 hpi. However,

413 the corresponding CCF2-AM correlation data exhibited a higher sensitivity for detecting
414 differences between Wt I-I vs. Wt U-I cells and yielded 81 significant deviants from the
415 Gaussian distribution (Fig. 5A, left panel). Of the deviants, 73 (~90.1%) fell in regions of
416 the scatterplot where genes were either: 1) negatively correlated with the CCF2-AM
417 ratio in one condition and positively correlated in the other; or 2) had stronger positive or
418 negative correlations in Wt U-I cells than in Wt I-I cells as determined by a Gaussian
419 model (Fig. 5A, left panel, blue regions; Table S4A). This provides evidence for
420 downstream events in infection (i.e., release of dense granule proteins, parasite
421 invasion) suppressing effects of genes induced by ROP injection as early as 2 hpi.

422 At 3 hpi, 122 DEGs and 423 CCF2-AM correlation deviants were identified for Wt
423 I-I vs. Wt U-I cells, pointing to a divergence in the injection vs. infection responses at
424 this later time point. Of the DEGs, 100 (~82.0%) exhibited opposing trajectories in Wt I-I
425 vs. Wt U-I cells (Table S3F), i.e., they were either: 1) upregulated in one cell type and
426 downregulated in the other compared to a common Wt U-U standard; or 2) more
427 upregulated or downregulated in Wt U-I cells compared to the standard than in Wt I-I
428 cells. In addition, of the CCF2-AM correlation deviants, 333 (~79%) exhibited at least a
429 moderate negative correlation with the CCF2-AM ratio in Wt I-I cells, an observation
430 consistent with these genes being downregulated in response to the combination of all
431 parasite-derived insults and effectors during infection (Fig. 5A, right panel; Table S4A).
432 Furthermore, 282 (~67%) of the deviants fell in regions of the scatterplot in which the
433 impact of ROPs is dampened by dense granule proteins (GRAs) and parasite invasion
434 (Fig. 5A, right panel, blue regions; Table S4A), which is consistent with host responses
435 in Wt U-I cells being counteracted by parasite effectors that are operating in Wt I-I cells

436 only. This lends further support to the notion that effectors injected circa invasion (i.e.,
437 ROPs) are counterbalanced by subsequently introduced effectors (i.e., GRAs). Of note,
438 the remaining 141 CCF2-AM deviant genes at 3 hpi fell within the sections of the
439 scatterplot in which the effects of ROPs are enhanced by those of the GRAs and
440 parasite invasion (Fig. 5A, right panel, yellow regions; Table S4A). This suggests that
441 while GRA release and parasite penetration may counterbalance some ROP-induced
442 host responses, these events may also enhance other genes induced by ROP injection.

443 To discern the biological significance of the differences between the infection vs.
444 injection responses, we performed GSEA on Wt U-I vs. Wt I-I DEGs. The resulting
445 enriched gene sets (Fig. 5B) included many that were previously identified in the host
446 infection response, with gene sets enriched from genes expressed higher in Wt I-I cells
447 corresponding to more inflammatory processes. Because the vast majority of genes
448 with higher expression in Wt U-I cells than in Wt I-I cells exhibited evidence of ROP
449 effectors being counteracted by subsequently secreted effectors such as MDGs and
450 MIGs (84 out of 93 genes; Table S3F), these findings are consistent with injection-
451 associated inflammatory host processes ramping up upon parasite penetration (and
452 GRA release), while other injection-associated processes are dampened by these later
453 events.

454

455 ***Parasite Effectors Counteract One Another to Yield a Modest Host Response to***
456 ***Early Parasite Infection***

457 Next, we sought to determine the contribution of individual parasite effector
458 compartments to the difference between the host infection (in Wt I-I cells) vs. ROP

459 injection (in Wt U-I cells) responses. Because Wt U-I and Wt I-I cells are both injected
460 with ROPs and originate from the same monolayer, ROPs and paracrine effectors likely
461 do not explain the differences between these two cell types. Instead, MDGs, MIGs, and
462 the act of parasite penetration itself are, *a priori*, most likely to explain these differences.
463 Our dataset, which includes infected (I-I), bystander uninfected (U-U), and U-I cells
464 originating from monolayers infected with wild type and $\Delta myr1$ parasites, presents a
465 unique opportunity to examine the impacts of these compartments in isolation.

466 To determine how individual effector compartments contribute to the
467 transcriptomic differences between Wt I-I vs. Wt U-I cells, we made two key
468 comparisons. In the first comparison, we examined Dmyr1 U-I cells, which presumably
469 respond to ROP injection, and Dmyr1 I-I cells, which are thought to respond to ROP
470 injection plus MIGs and parasite penetration (Fig. 1C; Fig. 1D). We predicted that MIGs
471 and parasite penetration would account for the differences between Dmyr1 I-I and
472 Dmyr1 U-I cells, and for a subset of the differences between Wt U-I and Wt I-I cells. In
473 the second comparison, we examined Wt I-I vs. Dmyr1 I-I cells, which originate from
474 monolayers infected with wild type and $\Delta myr1$ parasites, respectively. Signatures
475 detected in Dmyr1 I-I cells likely reflect the host response to the combination of ROP
476 injection, MIG activity, parasite penetration of host cells, and paracrine effectors
477 secreted into the extracellular milieu, while those detected in Wt I-I cells likely reflect the
478 response to these elements plus MDG secretion (Fig. 1C). Therefore, we predicted that
479 comparing Dmyr1 I-I vs. Wt I-I would illustrate the impact of MDGs, as well as any
480 paracrine effects dependent on the presence of MYR1 (Fig. 1D), and that this would

481 account for a second subset of the differences between the infection vs. injection
482 response showcased in the Wt I-I vs. Wt U-I comparison.

483

484 *MYR-Independent GRAs and Parasite Penetration Collectively Enhance ROP-induced*
485 *Inflammatory Responses*

486 To examine the host response to the combination of MIGs and parasite
487 penetration, we compared Dmyr1 U-I cells, which should be penetrated by ROPs, and
488 Dmyr1 I-I cells, into which parasites should secrete ROPs and MIGs, but not MDGs (Fig.
489 1C; Table S3G). At 2 hpi, only 5 DEGs and no GSEA enriched gene sets were identified,
490 implying profound similarity between Dmyr1 U-I and Dmyr1 I-I cells at this time point (as
491 was also the case for Wt U-I vs. Wt I-I cells). At 3 hpi, 80 DEGs were identified, pointing
492 to a slight divergence between these two cell types at this time point. 48 (60%) of the
493 DEGs exhibited evidence of being influenced by effectors that counteract one another's
494 effects (i.e., their expression exhibited either: 1) opposing trends in Dmyr1 U-I vs.
495 Dmyr1 I-I cells when compared to an uninfected Dmyr1 U-U standard; or 2) a stronger
496 induction or suppression in Dmyr1 U-I cells than in Dmyr1 I-I cells), which suggests that
497 MIGs may play a role in neutralizing the effects of the ROPs preceding them. Note,
498 however, that we cannot exclude the possibility that this effect is attributable to stimuli
499 related to physical penetration by the parasites.

500 GSEA of the 3 hpi DEGs identified 15 enriched gene sets (Fig. 6), of which 9
501 were also found to be enriched in the Wt U-I vs. Wt I-I comparison (Fig. 5B). For gene
502 sets enriched from genes expressed higher in Dmyr1 I-I cells than in Dmyr1 U-I cells,
503 nearly all corresponded to gene sets already identified as part of the host response to

504 ROP injection and/or were associated with inflammatory processes. In contrast, none of
505 the gene sets enriched from genes expressed higher in Dmyr1 U-I cells were identified
506 as part of the injection response and instead corresponded to other processes, i.e.,
507 complement cascade, coagulation, MTORC1 signaling, and myogenesis. Taken
508 together, these results suggest that MIGs and parasite penetration do indeed account
509 for some of the difference between the infection response (in Wt I-I cells) vs. the
510 injection response (in Wt U-I cells). More specifically, genes corresponding to
511 inflammatory processes that are already induced upon ROP injection (in Wt U-I and
512 Dmyr1 U-I cells) appear to be further induced, i.e., enhanced, by the combination of
513 MIGs and parasite penetration, while genes for which the effect of MIGs + Parasites
514 dampen the influence of the ROPs appear to correspond to a different set of cellular
515 processes. Although this latter set of genes accounts for the majority (60%) of Dmyr1 U-
516 I vs. Dmyr1 I-I DEGs, the majority of the total enriched gene sets corresponds to cellular
517 processes enhanced rather than dampened by MIGs + Parasites, and these enhanced
518 gene sets collectively exhibit much higher statistical significance. This raises the
519 possibility that at least some processes dampened by MIGs + Parasites may not be
520 adequately captured by the Hallmark gene sets.

521

522 *MYR-Dependent GRAs Counterbalance Parasite Effectors Released Earlier in the Lytic*

523 *Cycle*

524 A previously published bulk RNA-seq experiment comparing host transcription in
525 monolayers infected with wild type vs. $\Delta myr1$ parasites at 6 hpi (31) revealed a set of
526 genes such that in the absence of MYR1, expression changes were unmasked, while in

527 the presence of MYR1 (i.e., during wild type infection), there was no net change. This
528 work implies that collectively, MDGs and associated paracrine effectors secreted during
529 infection with wild type but not $\Delta myr1$ parasites participate in counterbalancing
530 transcriptional signatures induced by prior parasite-dependent stimuli.

531 To determine whether MDGs and associated paracrine effects play a similar role
532 in the present single cell datasets, and to ascertain their contribution to the difference
533 between the infection vs. injection responses, we compared Dmyr1 I-I and Wt I-I cells.
534 MAST analysis of this comparison identified 46 and 367 DEGs at 2 hpi and 3 hpi,
535 respectively (Table S3H). While GSEA of the 2 hpi DEGs returned no significantly
536 enriched gene sets, GSEA at 3 hpi revealed 16 significantly enriched gene sets, of
537 which all but one were enriched from genes expressed higher in Dmyr1 I-I cells than in
538 Wt I-I cells (Fig. 7A). Furthermore, 8 gene sets were identified in the previously
539 published bulk RNA-seq experiment comparing infections with wild type vs. $\Delta myr1$
540 parasites (31), while 6 corresponded to infection-associated gene sets (i.e., were
541 enriched from Wt I-I vs. Mock DEGs), and 8 were identified as part of the ROP injection
542 response (i.e., were enriched from Wt U-I vs. Wt U-U DEGs). Taken together, these
543 data are consistent with MDGs and/or their associated paracrine effects selectively
544 impinging on Wt I-I cells and dampening the effects of parasite effectors introduced into
545 host cells earlier in the lytic cycle. The overlap between these gene sets and those of
546 the injection response shows that some of the effectors whose responses were
547 dampened by MDGs and associated paracrine effects include injected effectors (i.e.,
548 ROPs), which was previously suspected (31) but never before explicitly demonstrated.

549 Though comparing Dmyr1 I-I vs. Wt I-I cells illustrates the collective impact of
550 MDGs and MYR-dependent paracrine effects on host transcription (Fig. 1D), this
551 comparison cannot distinguish the individual impacts of these two stimuli. To determine
552 the effect of MDGs alone, we performed CCF2-AM ratio correlation analysis on Wt I-I vs.
553 Dmyr1 I-I cells (Table S4B), as was performed for Wt I-I vs. Wt U-I. As was the case for
554 computation of both Wt I-I and Wt U-I CCF2-AM correlations, this type of analysis
555 excludes the impact of paracrine effects because each set of CCF2-AM correlation data
556 is computed using the CCF2-AM ratios of both I-I cells and U-U cells from the same
557 infected monolayer. 224 and 343 CCF2-AM ratio correlation deviants were identified
558 between Wt I-I and Dmyr1 I-I cells at 2 hpi and 3 hpi, respectively. 218 (~97.3%) and
559 297 (~86.6%) deviants at 2 hpi and 3 hpi, respectively, fell in the regions of the CCF2-
560 AM correlation scatterplot in which the impact of effectors found in Dmyr1 I-I cells (i.e.,
561 ROPs + MIGs) are dampened by effectors found in Wt I-I cells (i.e., MDGs; Fig. 7B, blue
562 regions; Table S4B), which implies that signatures induced by effectors released into
563 Dmyr1 I-I cells are counteracted specifically by MYR-dependent effectors released into
564 Wt I-I cells.

565

566 *MYR-Dependent Paracrine Effects Also Counterbalance Parasite Effectors Released*
567 *Earlier in the Lytic Cycle*

568 To determine the impact of specifically paracrine factors on the host response,
569 we examined two key comparisons: Wt U-U vs. Mock (which captures all paracrine
570 effects; Table S3I) and Dmyr1 U-U vs. Mock (which captures MYR-independent
571 paracrine effects; Table S3J). As illustrated in Fig. 1C and Fig. 1D, differences between

572 these two comparisons should be attributable to paracrine factors released from host
573 cells in a MYR-dependent fashion.

574 At both 2 hpi and 3 hpi, paracrine effects in $\Delta myr1$ parasite infections exhibited
575 robust differences from paracrine effects in wild type infections. At 2 hpi, ~196 and 54
576 DEGs were identified for the Dmyr1 and Wt cell comparisons, respectively; at 3 hpi, the
577 difference was even more pronounced, with 1,864 DEGs identified for the Dmyr1
578 comparison, vs. only 20 DEGs for Wt. In addition, GSEA of Dmyr1 U-U vs. Mock DEGs
579 exposed an abundance of gene sets, many of which corresponded to inflammatory
580 processes and other pathways found to be part of the infection response, whereas
581 GSEA of Wt U-U vs. Mock DEGs enriched for few, if any gene sets (3 and 0 at 2 hpi
582 and 3 hpi, respectively; Fig. 8A). Furthermore, the responses of these DEGs were
583 reproduced consistently between not only U-U cells vs. mock-infected cells, but also
584 between U-I or I-I cells vs. mock-infected cells (Fig. 8B), which establishes that these
585 trends affect all cell types within a given infected monolayer. Taken together, these
586 results suggest that gene expression trends induced during *Toxoplasma* infection (i.e.,
587 those encapsulated by the DEGs that arise from comparing Dmyr1 U-U and Mock cells),
588 including those corresponding to pathways that respond to injected ROPs, are
589 suppressed via a MYR-dependent paracrine mechanism. Accordingly, supernatants
590 taken from host cell cultures infected with wild type and $\Delta myr1$ could, in theory, exert
591 transcriptional influence on fresh host cell monolayers, an interesting avenue for future
592 investigation.

593

594 ***Model of Host Responses to Individual Toxoplasma Parasite-Dependent Stimuli***
595 ***and Effector Compartments***

596 The preceding analyses have accounted for host responses to 5 parasite-
597 dependent stimuli: 1) rhoptry protein (ROP) injection; 2) MYR-independent dense
598 granule (MIG) secretion; 3) MYR-dependent dense granule (MDG) secretion; 4)
599 paracrine effects (which can be further subdivided into MYR-independent vs. MYR-
600 dependent paracrine effects); and 5) parasite invasion. To succinctly represent the
601 interplay between these stimuli, we curated a list of gene sets that best represented the
602 expression trends captured in our analyses. Gene sets were included if they were
603 significantly enriched (false discovery rate < 0.25) from DEGs between a majority of the
604 following 8 key comparisons: 1) Wt U-I vs. Wt U-U (ROP injection); 2) Wt I-I vs. Dmyr1
605 I-I (MDGs + MYR-dependent paracrine effects); 3) Wt U-U vs. Dmyr1 U-U (MYR-
606 dependent paracrine effects); 4) Dmyr1 I-I vs. Dmyr1 U-I (MIGs + Parasite invasion); 5)
607 Dmyr1 U-U vs. Mock (MYR-independent paracrine effects); 6) Wt I-I vs. Wt U-I (MIGs +
608 MDGs + parasite invasion); 7) Wt I-I vs. Wt U-U (all stimuli except paracrine effects);
609 and 8) Wt I-I vs. Mock (all stimuli). The 12 gene sets selected included those pertaining
610 to immune responses, cell proliferation, cellular stress, and the complement pathway.
611 Expression trends for the DEGs within these gene sets are summarized in Fig. 9.

612 Based on our analyses, we propose the following model of parasite-driven effects
613 on host cell transcription. First, because Wt U-I cells appeared to induce DEGs in nearly
614 all the showcased gene sets compared to Wt U-U cells, ROP injection likely induces
615 many of the pathways these gene sets capture, particularly immune-related and cellular
616 stress pathways (Fig. 9A and Fig. 9B, ROPs; Fig. 9C, ROP injection). These signatures

617 may arise in response to the ROPs themselves, or due to cell trauma secondary to
618 perforation of the host cell membrane by the parasite during ROP injection. Next,
619 parasites penetrate the host cell and secrete MIGs into the PVM. The host response to
620 these two stimuli together is relatively mild, as evidenced by the high false discovery
621 rates and small number of genes per gene set, even at 3 hpi. Though MIGs + Parasites
622 appeared to counteract the effects of ROP injection at the *gene* level, their most
623 significant impact at the *gene set* level appears to be enhancement of inflammatory
624 transcriptional signatures induced by ROP injection (Fig. 9A and Fig. 9B, MIGs +
625 Invasion; Fig. 9C, MIG Secretion and Parasite Penetration). This does not exclude the
626 possibility that other host processes not covered by the Hallmark gene sets are
627 suppressed by MIGs + Parasites. Next, in cells infected with $\Delta myr1$ parasites, MYR-
628 independent paracrine factors secreted by neighboring infected cells appear to enhance
629 the effects of ROP injection even more so than MIGs + Parasites and may do so not
630 only for immune-related genes, but also for genes pertaining to cellular stress,
631 complement, and cellular proliferation (Fig. 9A and Fig. 9B, $\Delta myr1$ UU-mock/P(MI)). In
632 contrast, during wild type infections, two additional parasite-dependent stimuli, MDGs
633 and MYR-dependent paracrine factors, both appear to rein in transcriptional signatures
634 induced by the other stimuli (Fig. 9A and Fig. 9B, MDGs + P(MD); Fig. 9C, MYR-
635 dependent stimuli; Fig. 7B). Together, all five parasite classes produce transcriptional
636 signatures that veer toward induction of genes pertaining to inflammation and cellular
637 stress but that are less pronounced than the response to injection of ROPs.

638

639 **Discussion**

640 In this study, we examined host responses to infection with the parasite
641 *Toxoplasma gondii* using scRNA-seq on *in vitro* infected, uninfected, and uninfected-
642 injected (U-I) host cells, the latter of which arise from aborted invasion events and that
643 have until very recently (44) been characterized primarily morphologically. Key fixtures
644 of our experimental pipeline included: 1) early time points, to limit isolating false positive
645 U-I cells arising from mechanisms besides aborted invasion; 2) FACS sorts, which
646 purified rare U-I cells and relatively rare infected cells at early time points; and 3) single
647 cell resolution, which enabled bioinformatic validation of all cells' infection status. The
648 level of confidence lent by these measures to the validity of the captured U-I cells
649 enabled interrogation of host responses specifically to ROP injection, an aspect of
650 parasite infection previously inaccessible to study due to the rapid kinetics of effector
651 secretion at the time of invasion. Note that while others have also used scRNA-seq to
652 measure host responses to *Toxoplasma* infection at a single cell level, these studies
653 analyzed cells from animals at many days post-infection, and therefore did not assess
654 the earliest impacts of infection or particularly ROP injection (45).

655 Because the experimental pipeline also leveraged infections with $\Delta myr1$
656 parasites, our dataset is a comprehensive resource for the individual impacts of not only
657 ROPs, but also MIGs, MDGs, and paracrine stimuli on host transcription. Our analyses
658 revealed an early response to *Toxoplasma* infection with subtle yet clear signatures
659 overlapping with inflammatory and cellular stress signaling axes. Induction of these
660 axes appears to be 1) driven primarily by ROP injection; 2) enhanced somewhat by the
661 combination of MIGs, parasites, and MYR-independent paracrine factors; and 3)
662 counterbalanced by MDGs and downstream paracrine effects, i.e., factors secreted

663 during wild type but not $\Delta myr1$ infection. These findings substantiate previous evidence
664 that at least some MDGs suppress host responses induced by other parasite-driven
665 transcriptomic perturbations (31). They may also explain the recent finding that the
666 avirulent phenotype of $\Delta myr1$ parasites during *in vivo* mouse infections is rescuable by
667 co-infecting animals with both wild type and MYR1-deficient parasites (46); parasites
668 expressing MYR1 may induce host cells to secrete paracrine factors that suppress
669 transcription of inflammatory gene products that would otherwise limit $\Delta myr1$ parasite
670 infections. Note that while this manuscript was in preparation, a transcriptomic study of
671 U-I macrophages was published by Hunter and colleagues (44). While they used
672 different strains (Pru and CEP), looked at later time points (20-24 hpi), and did not look
673 at MYR1-dependent effects, their primary conclusions that U-I cells experience a major
674 impact of rhoptry effectors (in their case, specifically ROP16), and that paracrine effects
675 are also in play, are similar to the conclusions reached here.

676 Of note, the host response to MIGs + Parasites was especially subtle, given that
677 parasite invasion involves dramatic mechanical perturbations to host cells that might be
678 expected to trigger transcriptional responses. As we did not use host cells containing
679 MIGs and no parasites or vice versa, we could not discern the impact of the MIGs in
680 isolation. Nonetheless, it is tempting to speculate that the response to MIGs + Parasites
681 may reflect MIGs counteracting the effects associated with parasite penetration and
682 PVM formation, which may explain the subtle net inflammatory response.

683 In addition, the presence of ROPs and MDGs that respectively activate and
684 suppress certain host processes might be interpreted as energetically wasteful. Why
685 might *Toxoplasma*, an obligate intracellular organism likely under selective pressure for

686 transcriptional efficiency, expend extra resources on effectors that negate one other's
687 effects? One possibility is that ROPs may have undergone selection optimizing for
688 functions required to establish and protect the parasite's intracellular niche (4-9, 47-52),
689 but may also trigger unavoidable host responses detrimental to the parasite. In this
690 scenario, MDGs and paracrine effects could ameliorate such ROP-triggered side effects
691 while theoretically leaving processes beneficial to the parasite intact. Another possibility
692 is that ROPs and GRAs could grant *Toxoplasma* the ability to fine tune host responses
693 in terms of timing and/or magnitude, likely an advantage to an organism that must be
694 equipped to encounter a diversity of intracellular environments due to its extraordinarily
695 broad host range (1, 53, 54).

696 Our analysis also reveals a striking effect on the host cell cycle, in which U-I cells
697 exhibit enrichment of G2/M phase cells. Curiously, this enrichment appeared not to be
698 preserved at 3 hpi, which suggests that the responsible parasite factors exert only a
699 transient influence on host cell cycle-related genes. Of the parasite effectors currently
700 known to modulate the host cell cycle (19, 22, 23, 40, 55), ROP16 is most likely to
701 explain these results: ROP16 phosphorylates ubiquitin-like containing PHD and RING
702 finger domain 1 (UHRF1) in a manner that peaks at 3 hpi, which leads to epigenetic
703 silencing of cyclin B1 (40), a component of the cyclin B1/Cdk1 complex required for the
704 G2/M transition. However, ROP16 is likely not the only ROP to impinge on the host cell
705 cycle, as comparison of G1 phase U-I vs. U-U cells also revealed enrichment in the p53
706 Pathway and KRAS Signaling Up gene sets (Fig. 4; Fig. 9A and Fig. 9B, ROPs), whose
707 corresponding pathways promote cell cycle progression. Further analysis of U-I cells

708 from yet more time points and particularly those not in G1 may shed more light on this
709 interplay.

710 Finally, our analyses thus far reflect a fraction of the possible uses of our dataset,
711 which includes variables of time, parasite strain, infection status, cell cycle phases, and
712 UMAP populations. For example, our dataset includes reads not only from host cells but
713 also the *Toxoplasma* parasites, rendering the data a co-transcriptomic resource that will
714 likely illuminate novel host-parasite interactions. Furthermore, because of limiting
715 numbers, the analyses described here dealt primarily with G1 phase cells in UMAP
716 population 1 and largely excluded cells in the remaining cell cycle phases and UMAP
717 populations. The raw and processed transcriptomic data for these remaining cells,
718 including the results of differential gene expression analysis and of gene set enrichment
719 analysis, are publicly available (as are the data described thus far) on the Gene
720 Expression Omnibus under accession number GSE145800. Future analyses of such
721 cells may reveal roles for cell cycle phase, host cell type, or other host-dependent
722 processes.

723

724 **Materials and Methods**

725 Cell and Parasite Culture

726 All *Toxoplasma gondii* strains were maintained by serial passage in human
727 foreskin fibroblasts (HFFs) cultured at 37°C in 5% carbon dioxide (CO₂) in complete
728 Dulbecco's Modified Eagle Medium (cDMEM) supplemented with 10% heat-inactivated
729 fetal bovine serum (FBS), 2 mM L-glutamine, 100 U/ml penicillin, and 100 µg/ml
730 streptomycin.

731

732 Construction of Parasite Strains

733 RH Tfn-BLA TdTomato parasites were constructed by transfecting $\sim 10^7$ RH
734 Toxofilin-HA-beta-lactamase (RH Tfn-BLA) parasites (8) with the plasmid pSAT1::Cas9-
735 U6::sgUPRT (56) and with the linearized pCTR_{2T} plasmid containing the construct to
736 express TdTomato (57) using the AMAXA Nucleofector 4D system (U-033 setting) and
737 the P3 primary cell 4D-nucleofector X kit with the 16-well nucleocuvette strip (Lonza,
738 V4XP-3032). Clones were obtained by FACS using the FACS Aria II sorter at the
739 Stanford Shared FACS Facility for the brightest red parasites and single cloning the
740 TdTomato+ enriched population by limiting dilution into 96-well plates.

741 A CRISPR-Cas9 strategy was used to construct RH $\Delta myr1$ mCherry Tfn-BLA
742 parasites from an RH $\Delta myr1$ mCherry parental strain (25). The parental strain was
743 transfected with the plasmid pSAG1::Cas9-U6::sgUPRT and a linear construct that
744 contained Toxofilin-HA-Beta-lactamase (Tfn-HA-BLA) expressed under *toxofilin*'s
745 endogenous promoter. The Tfn-HA-BLA construct was PCR amplified from the plasmid
746 SP3 (8) such that the final amplicon was flanked by 20 nucleotide (nt) homology arms to
747 the *UPRT* gene that are identical to those used to target constructs to the *UPRT* locus
748 in (56). 15 μ g of pSAG1::Cas9-U6::sgUPRT and 3 μ g of the Tfn-HA-BLA linear
749 amplicon were transfected into $\sim 10^7$ parental strain parasites using the AMAXA
750 Nucleofector 4D system as described above, except the setting on the nucleofector (T-
751 cell human unstimulated HE setting). Selection for parasites with 5 μ M 5-
752 fluorodeoxyuridine (FUDR) began at 1 day post-transfection and proceeded for 3 lytic
753 cycles in monolayers of human foreskin fibroblasts (HFFs). The transfected, selected

754 parasite populations were subjected to two rounds of single cloning, one to generate
755 populations of parasites enriched for the presence of the Tfn-HA-BLA construct, and
756 one to purify for individual parasite clones containing the construct, where the readout
757 for the presence of the construct was cleavage of the BLA-cleavable FRET-based dye
758 CCF2-AM, which results in a fluorescence color shift.

759 IFA of monolayers infected with newly constructed RH $\Delta myr1$ mCherry Tfn-BLA
760 parasites was used to validate correct localization of the Tfn-HA-BLA construct to the
761 parasite rhoptry organelles and the absence of expression of host factors known to be
762 induced in the host nucleus as a result of MYR-dependent GRAs. Coverslips seeded
763 with confluent HFF monolayers were infected with putative RH $\Delta myr1$ mCherry Tfn-BLA
764 clones for ~24 hours, fixed in 4% formaldehyde for 20 minutes, permeabilized in 0.2%
765 Triton X-100 for 20 minutes, blocked in 1x PBS containing 3% bovine serum albumin (3%
766 BSA solution) for 1 hour at room temperature, stained with primary and secondary
767 antibodies in 3% BSA solution, and mounted onto glass slides using DAPI-containing
768 VectaShield (Vector Laboratories, H-1200) and sealed with colorless nail polish. For
769 Tfn-HA-BLA localization, primary antibodies were mouse-anti-ROP2/3/4 (1:250 dilution,
770 4A7, (58)) and rat anti-HA (1:500, clone 3F10, Sigma Aldrich, 11867431001), and
771 secondary antibodies were goat anti-mouse IgG-Alexa 647 (1:2000 dilution, Thermo
772 Fisher, A-21235) and goat anti-rat IgG-Alexa 488 (1:2000 dilution, Thermo Fisher, A-
773 11006). To verify the absence of the MYR1 protein, the primary antibody rabbit anti-c-
774 myc (1:600 dilution, Sigma, M5546) and the secondary antibody goat anti-rabbit IgG-
775 Alexa 594 (1:2000 dilution, Thermo Fisher, A-11012) were used, and coverslips were
776 seeded with either >3-week-old confluent HFF monolayers or with younger monolayers

777 that had been serum starved for at least 24 hours (using 0.5% FBS instead of 10% FBS
778 in the culture medium) to ensure no spurious induction of c-myc in uninfected host cells.
779 Only clones where the anti-HA and anti-ROP2/3/4 signal colocalized and where no
780 expression of c-myc was detected in the infected host nucleus were selected. RH Tfn-
781 HA-BLA TdTomato parasites (32) and the parental RH $\Delta myr1$ mCherry parasites were
782 also subjected to both protocols as positive and negative controls, respectively.
783 Coverslips were imaged either on the Stanford Neuroscience Imaging Service core's
784 Zeiss LSM 710 confocal microscope or on an Olympus BX60 upright fluorescence
785 microscope.

786 Western blot was used to verify for the correct size of the Tfn-HA-BLA fusion
787 protein expressed in RH $\Delta myr1$ mCherry Tfn-BLA parasite clones. Lysates were
788 generated by treatment of parasite pellets with SDS-PAGE loading dye containing 10%
789 beta-mercaptoethanol. The lysates were separated by SDS-PAGE and transferred to a
790 PVDF membrane, and the membrane was blocked with TBST (TBS, 0.05% Tween-20)
791 containing 5% milk for 1.25 hours. The membrane was incubated with horseradish
792 peroxidase (HRP)-conjugated rat anti-HA (clone 3F10) monoclonal antibodies (Roche,
793 Indianapolis, IN) at a dilution of 1:5,000 for 2 hours, and with 1:10,000 dilution rabbit
794 anti-SAG1 for 30 minutes followed by 1:20,000 dilution goat anti-rabbit-HRP for 30
795 minutes, and developed using the ECL Prime Western Blotting System (Sigma-Aldrich,
796 RPN2232).

797

798 Determination of Time to Division for Infected 10 T1/2 Cells

799 To determine the time post-infection at which infected 10 T1/2 cells divided, 10
800 T1/2 host cell monolayers were infected with RH Tfn-BLA TdTomato parasites, and the
801 infected monolayers were imaged by time lapse microscopy.

802 To prepare the parasites for the infection, the parasites were released from
803 heavily infected monolayers of HFFs by mechanical disruption of the monolayers using
804 sterile, disposable scrapers and passage at least 6 times through a 25 gauge syringe.
805 The parasites were washed by pelleting out HFF debris (133.5-208.5 x g for 5 minutes)
806 and resuspending the parasite pellet generated by spinning the remaining supernatant
807 469.2 x g in phenol red-negative low serum DMEM.

808 To prepare the host cell monolayers, 10 T1/2 cells approximately 1 week from
809 their date of thaw were seeded into 12-well tissue culture plates at approximately 6.0×10^4 ,
810 1.2×10^5 , and 2.4×10^5 cells per well. The 10 T1/2 cells were then incubated for >2
811 hours in cDMEM, serum starved by incubation at 37°C in 5% CO₂ in low serum DMEM
812 (i.e., cDMEM containing 0.5% FBS instead of 10% FBS) for 23 hours, washed and
813 stained with 500 µl of Cell Tracker Green CMFDA (CTG-CMFDA; Thermo Fisher,
814 C2925) diluted 1:1000 in prewarmed PBS for 30 minutes at 37°C in 5% CO₂, and
815 washed and incubated in phenol red-negative low serum DMEM (Thermo Fisher,
816 31053028) for 30 minutes. At 24 hours post-infection, RH Tfn-BLA TdTomato parasites
817 were added to the monolayers at a multiplicity of infection (MOI) of 6.

818 Time lapse, epifluorescence images of the infected monolayers were acquired
819 over 16 hours in a controlled (37°C and 5% CO₂) environment using a Nikon Eclipse
820 inverted microscope (Julie Theriot lab). Images were acquired every 20 minutes using
821 100 ms of exposure at 25% power for the Phase, mCherry (to visualize parasites), and

822 GFP (to visualize host cytoplasmic CTG-CMFDA) channels. Cells that were uninfected
823 at the start of the time lapse were followed to determine whether they were infected by
824 the end of the time lapse, as determined by: 1) clearing of cytoplasmic CTG-CMFDA in
825 the exact position of the parasite, 2) disappearance of birefringence in the Phase
826 channel upon parasite invasion, and c) the parasite tracking with the cell at all time
827 points following presumed infection. For each cell for which the precise moment of
828 infection was captured in the live video footage, the time to division was determined
829 using the time the cell was infected as the start time and the time the cell divided (if
830 applicable) as the end time.

831

832 FACS of Single Uninfected-Injected (U-I) and Control Cells for Single Cell RNA

833 Sequencing (scRNA-seq)

834 *Preparation of Single Cells for FACS Sorting*

835 To generate U-I cells for FACS sorting, 10 T1/2 host cells approximately 1 week
836 from their date of thaw were seeded into 6-well tissue culture plates at a density of
837 approximately 2.6×10^5 cells per well, incubated for >2 hours in cDMEM, and serum
838 starved by incubation in low serum DMEM (i.e., cDMEM containing 0.5% FBS instead of
839 10% FBS) for 24 hours. 10 T1/2 host cells were chosen as they are monolayer-forming,
840 contact-inhibited fibroblasts that are also suitable for single cell sorting due to adequate
841 dissociation into individual cells by a combination of mechanical and chemical disruption.
842 Next, either RH Tfn-BLA TdTomato or RH $\Delta myr1$ mCherry Tfn-BLA parasites were
843 released from heavily infected monolayers of HFFs by mechanical disruption of the
844 monolayers using sterile, disposable scrapers and passage at least 6 times through a

845 25 gauge syringe. Parasite-free lysate was similarly generated by mechanical disruption
846 of uninfected HFFs. Parasites and parasite-free lysate were washed by pelleting out
847 HFF debris (133.5-208.5 x g for 5 minutes) and resuspending the parasite pellet
848 generated by spinning the remaining supernatant 469.2 x g in low serum DMEM
849 containing either 1 μ M DMSO (for the wild type and $\Delta myr1$ conditions) or with 1 μ M of
850 the invasion inhibitor cytochalasin D (cytD, for the cytD-treated wild type condition),
851 incubated at room temperature for 10 minutes, and applied to the serum starved 10
852 T1/2 monolayers at multiplicity of infection (MOI) = 6, which maximized the abundance
853 of U-I cells in tissue culture. All 10 T1/2 monolayers were spun at 469.2 x g for 5
854 minutes to synchronize parasite contact with the monolayer. Infections were allowed to
855 proceed for 30 minutes, 1.5 hours, or 2.5 hours at 37°C. Because cytD is a reversible
856 inhibitor, extra cytD-containing low serum DMEM was added to each of the drug-treated
857 infections to maintain the concentration of cytD at 0.5-1 μ M for the entire infection
858 duration.

859 To identify host cells injected by parasite proteins, a 6x stock solution of the beta-
860 lactamase substrate CCF2-AM (Thermo Fisher, K1032) was added to the media over
861 10 T1/2 cells so that the final concentration of CCF2-AM was 1x. CCF2-AM treated
862 monolayers were incubated under foil (to protect from light) for 30 minutes at room
863 temperature (to prevent breakdown of CCF2-AM, which degrades at 37 °C), bringing up
864 the total infection duration to 1 h, 2 h, and 3 h.

865 To harvest the 10 T1/2 monolayers for subsequent FACS analysis, the
866 monolayers were: 1) washed 3 times in 1x phosphate buffered saline (PBS) to remove
867 any HFF debris adhering to the monolayer; 2) incubated in trypsin (prepared in plastic

868 vessels only) at room temperature for 6-10 minutes; 3) quenched in an equal volume of
869 FACS buffer (1 x PBS + 2% FBS + 50 mM MgCl₂*6H₂O + 50 µg/ml DNase I); 4) passed
870 3 times through an 18 gauge syringe to break any residual cell clumps; and 5) washed
871 in FACS buffer to remove excess trypsin. Of note, DNase I and MgCl₂ were included in
872 the FACS buffer to prevent clumping of cells from cell death. The cells were then
873 stained with a viability dye and an extracellular parasite stain by 1) resuspending them
874 in 500 µl of chilled 4°C 1x PBS containing 3% bovine serum albumin (BSA) and 1:500
875 dilution rabbit anti-SAG2A primary antibody (gift of C. Lekutis) for 30 minutes on wet ice,
876 2) washing them in 5 ml of ice cold 1x PBS and spinning at 133.5 x g (lowest setting) at
877 4°C for 5 minutes, and 3) resuspending the pellets in chilled 1x PBS containing 3% BSA,
878 1:1000 dilution goat anti-rabbit IgG-Alexa 647 (Thermo Fisher), and 3 µl/ml near-
879 infrared live/dead fixable viability dye (Thermo Fisher, L94375) for 30 minutes on wet
880 ice. Samples were then washed as before, the pellets were resuspended in 1 ml of
881 chilled FACS buffer, and the cell suspension was transferred through a nylon filter cap
882 (Thomas Scientific, 4620F40) into polypropylene FACS tubes stored on wet ice and
883 protected from light until FACS sorting.

884

885 *FACS of Single Cells*

886 To prepare the multi-well lysis plates into which cells were deposited during
887 FACS sorting, lysis buffer was dispensed either by the Mantis liquid handling robot
888 (Formulatrix) at 0.4 µl per well into 384-well hard shell low profile PCR plates (Bio-rad)
889 for single cell RNA sequencing, or by hand at 5 µl per well into 96-well hard shell low
890 profile PCR plates (Bio-rad) for bulk RNA sequencing. Lysis buffer was prepared in

891 batches of 8 ml by mixing 5.888 ml water, 160 μ l recombinant RNase inhibitor (Takara
892 Clontech), 1.6 ml of 10 mM dNTP (Thermo Fisher), 160 μ l of 100 μ M oligo-dT (iDT),
893 1:600,000 diluted ERCC spike-in RNA molecules (Thermo Fisher), and 32 μ l 10% Triton
894 X-100. All reagents were declared RNase free. Lysis plates were prepared the night
895 before each FACS sort, stored overnight at -80°C, and kept on dry ice during the FACS
896 sort.

897 All host cell samples were sorted at the Stanford Shared FACS Facility (SSFF)
898 by the BD Influx Special Order sorter using the following channels: forward scatter (488
899 nm blue laser, SSC detector), side scatter (488 nm blue laser, FSC detector), BV421
900 (405 nm violet laser, V460 detector, which detected cleaved CCF2-AM), BV510 (405
901 nm violet laser, V520 detector, which detected uncleaved CCF2-AM), mCherry (561 nm
902 yellow laser, Y610 detector, which detected parasite-associated cells), APC (640 nm
903 red laser, R670 detector, which detected the extracellular parasite stain vs. anti-SAG2A),
904 and APC-Cy7 (640 nm red laser, R750 detector, which detected dead cells). Gating
905 strategy used to obtain U-I, I-I, and U-U cells is indicated in Fig. 2B. More specifically,
906 cells without red fluorescence (i.e., parasite-free) but with enhanced signal from cleaved
907 CCF2-AM (i.e., injected) were sorted as U-I cells, while those with red fluorescence (i.e.,
908 parasite-associated), enhanced signal from CCF2-AM (i.e., injected), and low
909 extracellular parasite stain were sorted as I-I cells. Of note, the parasite-associated gate,
910 from which I-I cells were obtained, was intentionally kept narrow to ensure host cells
911 were each infected with approximately one parasite apiece, which limited confounding
912 downstream analysis with penetration of >1 parasite at two different time points. Single
913 color and colorless controls were used for compensation and adjustment of channel

914 voltages. Fluorescence data were collected with FACSDiva software and analyzed with
915 Flowjo software. Cells were index sorted such that each cell's fluorescence data were
916 recorded for subsequent analysis. For single cell experiments, cells were sorted into the
917 384-well lysis plates at 1 cell per well. For bulk experiments, cells were sorted into 96-
918 well lysis plates at 50-100 cells per well. Plates were sealed with foil plate sealers and
919 immediately placed on dry ice until the completion of the sort. Plates were then stored at
920 -80°C until library preparation.

921

922 cDNA Synthesis from Single Cell RNA, Library Preparation, and Sequencing

923 To convert the RNA obtained from single cells and bulk samples to cDNA, we
924 employed the Smart-seq2 protocol (59). For single cell library preparation, the liquid
925 handling robots Mantis (Formulatrix) and Mosquito (TTP Labtech) were employed to
926 transfer and dispense small volumes of reagents, and final reaction volume was 2 μ l per
927 well. For bulk sample library preparation, liquid handling was performed with standard
928 multichannel pipets and final reaction volume was 25 μ l per sample. cDNA was subject
929 to 19 round of pre-amplification and then quantified using EvaGreen and diluted in EB
930 buffer to obtain a final concentration of 0.4-0.8 ng/ μ l per sample. Library preparation
931 continued using in-house Tn5 tagmentation. For single cell libraries, we used custom
932 barcoded indices for each cell, and for bulk libraries, we used Nextera XT indices.
933 Libraries were submitted to the Chan Zuckerberg Biohub Genomics Core for
934 sequencing. Single cell libraries were sequenced on the NovaSeq 6000 by 2x150 base
935 pair paired end sequencing aiming at ~1 million reads per cell. Bulk libraries were

936 sequenced on the NextSeq by 2x150 base pair paired end sequencing at ~10 million
937 reads per sample.

938

939 Sequencing Alignment

940 Reads output from sequencing were aligned to a concatenated genome
941 composed of the mouse genome (GRCm build 38) and the GT1 *Toxoplasma gondii*
942 genome (ToxoDB version 36), which is the most complete reference for type I parasite
943 strains such as the RH strains used in this work. Alignment was performed using STAR,
944 and transcript counting was performed by Htseq-count, with standard parameters used
945 for both packages. A custom python script was used to sum transcript counts to yield a
946 final gene count matrix consisting of all sequenced cells and the number of read counts
947 detected for each gene.

948

949 Data Preprocessing

950 To filter out cells of poor quality from the analysis, we excluded cells based on
951 the following metrics: gene count, total read sum, percentage of reads that mapped to
952 the mouse-*Toxoplasma* concatenated genome, percentage of reads derived from
953 spiked in ERCC standards, and percentage of reads derived from ribosomal RNA.

954 The gene count matrices were then normalized as counts per median (cpm).
955 Briefly, we first calculated the sum of reads for all cells. We then divided the read counts
956 by the corresponding sum of reads in each cell and multiplied the fractional count by the
957 median of the sum of reads as a scaling factor. Normalized data were transformed to
958 log₂ space after adding a pseudo-count of 1 for each gene of each cell.

959 To determine the detection limit of each experimental trial (e.g., the 50%
960 detection rate), we computed a logistic regression model from a plot of the detection
961 probability for spiked-in ERCC standards. We then excluded genes where less than 5
962 cells in the experimental trial expressed that gene at a level above the detection limit.

963 To identify host genes associated with infection, we first excluded mouse genes
964 to which *Toxoplasma* sequences erroneously map (Table S1) by aligning RNA
965 sequences obtained from single cell extracellular RH parasites to the concatenated
966 mouse-*Toxoplasma* genome and eliminating all mouse genes with an average
967 $\log_2(\text{cpm}+1)$ expression of 0.2 or greater.

968

969 Single Cell vs. Bulk Sample Correlation Analysis

970 To validate the single cell expression data, we plotted the \log_2 mean expression
971 of each differentially expressed gene, as identified by the MAST algorithm using the
972 single cell data, in single cells vs. bulk samples. The sklearn package was applied to
973 compute linear regression and the corresponding R^2 (coefficient of determination)
974 values.

975

976 Cell Cycle Analysis and Annotation

977 To predict the cell cycle phase of individual single cells, we curated a list of 175
978 cell cycle marker genes from the literature (60-67) and from the database CycleBase
979 3.0 (68). We computed the first two principle components of the gene count matrix using
980 principle component analysis (PCA) and projected the cells. We partitioned the cells
981 using K-Means clustering and assigned the clusters with their predicted cell cycle

982 phases (G1, S, and G2/M) based on the expression of 175 cell cycle marker genes
983 curated from the literature (Table S2).

984

985 Dimensionality Reduction

986 To visually represent relationships between single cells across all experimental
987 trials based on their transcriptional variation regardless of experimental conditions, we
988 identified and filtered for the top 1000 genes with the highest dispersion (i.e., the genes
989 with the most variable expression for their bin groups with similar expression level)
990 across all datasets, applied mutual nearest neighborhood batch correction (MNNPY) to
991 correct for batch effects, and projected the data onto two dimensional space with the
992 uniform manifold approximation and projection (UMAP) algorithm using default
993 parameters in Scanpy (69). Leiden clustering using the top 1000 dispersed genes
994 enabled partitioning of cells into three populations (1, 2, and 3), which we separated into
995 individual datasets for downstream analysis.

996

997 Infection Status Classification

998 We also determined the host infection load by quantifying the percent of reads
999 that mapped to *Toxoplasma* in a given sample. We filtered samples which were shown
1000 by FACS to exhibit one presumed infection status (based on red fluorescence from
1001 internalized parasites) but were determined to exhibit the opposite or an ambiguous
1002 infection status otherwise (based on percentage of reads derived from *Toxoplasma*).

1003

1004 Differential Expression Analysis

1005 To obtain differentially expressed genes (DEGs) between all pairs of conditions,
1006 we used the Model-based Analysis of Single Cell Transcriptomics (MAST) algorithm (70)
1007 to compute the results on all G1, correctly classified, and UMAP population 1 cells. We
1008 used the default settings except with an adaptive conditional mean of expression based
1009 on 20 number of bins, at least 30 genes in each bin, and we did not filter out any gene
1010 with non-zero expression frequency in the samples.

1011

1012 Gene Set Enrichment Analysis

1013 We performed gene set enrichment analysis (GSEA) on the lists of differentially
1014 expressed genes between all pairs of experimental conditions, ranked by their relative
1015 expression in each of the two conditions, for each individual experimental trial using the
1016 fast pre-ranked gene set enrichment analysis (fgsea) package (71). Genes were
1017 compared to the Molecular Signature Database's Hallmarks gene sets. Pathways with
1018 an adjusted p-value, i.e., false discovery rate (FDR) of < 0.25 were considered to be
1019 significantly enriched at the top or the bottom of the ranked list of differentially
1020 expressed genes.

1021

1022 Identification of Differentially Regulated Genes between Conditions Using CCF2-AM

1023 Ratio Correlation Analysis

1024 To identify host genes associated with injection, we first computed the CCF2-
1025 ratio for each cell, a metric that serves as a readout for parasite effector injection and
1026 that was calculated by dividing the log-transformed cleaved CCF2-AM fluorescence by
1027 the log-transformed uncleaved CCF2-AM fluorescence. Next, we excluded mouse

1028 genes below the detection limit and mouse genes to which *Toxoplasma* sequences
1029 erroneously map. Finally, for each infected or injected condition (i.e., Wt U-I, Wt I-I,
1030 Dmyr1 U-I, Dmyr1 I-I, CytD U-I, and CytD I-I), we computed the Spearman correlation of
1031 each of the remaining genes to the CCF2-AM ratio using cells from the condition of
1032 interest and cells from the cognate U-U condition (e.g., to calculate Spearman
1033 correlations for Wt U-I cells, we correlated gene expression to the CCF2-AM ratio in Wt
1034 U-I and Wt U-U cells).

1035 To identify genes differentially regulated between pairs of conditions using the
1036 CCF2-AM correlation data, we generated scatterplots where each data point
1037 represented a gene and its displacement on each of the x- and y-axes represented the
1038 Spearman correlation in each of the conditions. We modeled a Gaussian distribution
1039 using the Sklearn package with default parameters with settings "n_components=1" and
1040 "covariance_type='full'". Genes with a difference in CCF2-AM correlation score of >0.2
1041 or <-0.2 and whose probability densities were more than three standard deviations from
1042 the mean probability density were considered to exhibit significant differential
1043 expression between the pair of conditions under scrutiny.

1044

1045 Generation of Strip Plots

1046 Strip plots in Fig. 8B were generated using seaborn's catplot and boxplot
1047 packages to plot the normalized expression scores for each cell across 11 experimental
1048 conditions for differentially expressed genes (DEGs) between Dmyr1 U-U and Mock
1049 samples. The normalized expression score for each cell was calculated by 1)
1050 subtracting the minimum log₂ cpm for that gene across all cells in the experiment, 2)

1051 dividing the difference by the maximum log₂ cpm across all cells, such that the cell with
1052 the lowest count received a score of 0 and the cell with the highest count received a
1053 score of 1, and 3) computing the average of the normalized cpm's for each cell.

1054

1055 Generation of Bubble Plots

1056 Bubble plots in Fig. 9A and Fig. 9B were generated using a custom Python script
1057 in which columns indicated the gene set and rows indicated the comparison (taken to
1058 signify the impact of one to a few parasite-dependent stimuli on host transcription) from
1059 which the gene sets were enriched. The bubbles in each plot were color coded and
1060 sized based on one of two schemes. In the first scheme, bubble color indicated the
1061 normalized enrichment score, where scores were positive if the genes corresponding to
1062 a given gene set were expressed higher in the first member of the pair in the given
1063 comparison than in the second member of the pair, and bubble size indicated the
1064 significance (i.e., false discovery rate, or FDR) of the enrichment, where the absolute
1065 size of each bubble corresponded to the reciprocal of the FDR. In the second scheme,
1066 bubble color indicated the log₂ normalized fold change in expression of DEGs from a
1067 given comparison that also corresponded to a given Hallmark pathway, where positive
1068 fold changes indicated genes were expressed higher in the first member of the pair in
1069 the comparison than in the second member, and bubble size indicated the number of
1070 DEGs used to calculate the fold change. To calculate fold change for each given
1071 comparison's gene set, DEGs from the comparison that fell under the gene set were
1072 identified, expression of these DEGs in cpm was normalized across all cells to a
1073 maximum value of 1 and averaged across all the cells in each condition, and average

1074 normalized expression in the first experimental condition was divided by average

1075 normalized expression in the second experimental condition.

1076

1077 Data Availability

1078 The RNA sequencing dataset produced in this study has been uploaded in its
1079 entirety to the National Center for Biotechnology Information (NCBI) Gene Expression
1080 Omnibus (GEO) database under accession number GSE145800. The dataset includes
1081 the raw fastq files, processed gene count files (in counts per median), an anndata file
1082 containing the processed gene count files and other metadata such as the cell cycle
1083 phase and percentage of *Toxoplasma*-derived reads for each cell, and results of
1084 differential gene expression analysis and gene set enrichment analysis for up to eleven
1085 distinct species of host cell (i.e., Wt U-I, Wt I-I, Wt U-U, Dmyr1 U-I, Dmyr1 I-I, Dmyr1 U-
1086 U, CytD U-I, CytD I-I, CytD U-U, Mock, and CytD Mock) at each of three time points (i.e.,
1087 1, 2, and 3 hours) post-infection. Here, Wt, Dmyr1, and CytD designate host cells
1088 arising from monolayers infected with wild type (RH Tfn-BLA TdTomato), $\Delta myr1$ (RH
1089 $\Delta myr1$ mCherry Tfn-BLA) or cytochalasin D-treated wild type parasites, respectively,
1090 while Mock and CytD Mock refer to cells arising from monolayers mock-infected with
1091 parasite-free lysate (where the lysate was pretreated with cytochalasin D in the CytD
1092 Mock condition).

1093

1094 **Acknowledgments**

1095 Special thanks to Terence Theisen for his assistance in preparing U-I cells for
1096 FACS sorting; Dr. Anita Koshy for her careful reading of the manuscript; Meredith

1097 Weglarz and Marty Bigos from the Stanford Shared FACS Facility for their assistance
1098 during the FACS sorts for U-I cells; and David Parks and Catherine Carswell-Crumpton
1099 for their input in optimizing the FACS sort conditions to obtain pure U-I cell populations.
1100 We also thank Saroja Kolluru and Robert Jones for their assistance during library
1101 preparation and sample submission; Fabio Zanini for experimental suggestions; Geoff
1102 Stanley and Michelle Chen for their input on the bioinformatic analysis of the U-I
1103 scRNAseq data; and Julie Theriot, Zhou Xiaoxue, and Matthew J. Footer for their
1104 assistance with the live video microscopy experiments. This work was supported by NIH
1105 F30 AI124589-03 (SR), Stanford Interdisciplinary Graduate Bio-X Fellowship (YX), RO1
1106 AI021423 and AI129529 (JCB), Chan Zuckerberg Biohub (SRQ), NIH S10 Shared
1107 Instrument Grant S110RR025518-01 (Stanford Shared FACS Facility), and NIH
1108 NS069375 (Neuroscience Microscopy Core).

1109

1110 REFERENCES

- 1111 1. J. P. Dubey CPB. 1988. Toxoplasmosis of Animals and Man. CRC Press, Boca Raton.
- 1112 2. Blader IJ, Coleman BI, Chen CT, Gubbels MJ. 2015. Lytic Cycle of *Toxoplasma gondii*: 15
1113 Years Later. *Annu Rev Microbiol* 69:463-85.
- 1114 3. Rastogi S, Cygan AM, Boothroyd JC. 2019. Translocation of effector proteins into host
1115 cells by *Toxoplasma gondii*. *Curr Opin Microbiol* 52:130-138.
- 1116 4. Fleckenstein MC, Reese ML, Konen-Waisman S, Boothroyd JC, Howard JC, Steinfeldt T.
1117 2012. A *Toxoplasma gondii* pseudokinase inhibits host IRG resistance proteins. *PLoS Biol*
1118 10:e1001358.

- 1119 5. Reese ML, Shah N, Boothroyd JC. 2014. The Toxoplasma Pseudokinase ROP5 Is an
1120 Allosteric Inhibitor of the Immunity-related GTPases. *J Biol Chem* 289:27849-58.
- 1121 6. Etheridge RD, Alaganan A, Tang K, Lou HJ, Turk BE, Sibley LD. 2014. The Toxoplasma
1122 pseudokinase ROP5 forms complexes with ROP18 and ROP17 kinases that synergize to
1123 control acute virulence in mice. *Cell Host Microbe* 15:537-50.
- 1124 7. Li JX, He JJ, Elsheikha HM, Chen D, Zhai BT, Zhu XQ, Yan HK. 2019. Toxoplasma gondii
1125 ROP17 inhibits the innate immune response of HEK293T cells to promote its survival.
1126 *Parasitol Res* 118:783-792.
- 1127 8. Lodoen MB, Gerke C, Boothroyd JC. 2010. A highly sensitive FRET-based approach
1128 reveals secretion of the actin-binding protein toxofilin during Toxoplasma gondii
1129 infection. *Cell Microbiol* 12:55-66.
- 1130 9. Delorme-Walker V, Abrivard M, Lagal V, Anderson K, Perazzi A, Gonzalez V, Page C,
1131 Chauvet J, Ochoa W, Volkmann N, Hanein D, Tardieux I. 2012. Toxofilin upregulates the
1132 host cortical actin cytoskeleton dynamics, facilitating Toxoplasma invasion. *J Cell Sci*
1133 125:4333-42.
- 1134 10. Ong YC, Reese ML, Boothroyd JC. 2010. Toxoplasma rhoptry protein 16 (ROP16)
1135 subverts host function by direct tyrosine phosphorylation of STAT6. *J Biol Chem*
1136 285:28731-40.
- 1137 11. Yamamoto M, Standley DM, Takashima S, Saiga H, Okuyama M, Kayama H, Kubo E, Ito H,
1138 Takaura M, Matsuda T, Soldati-Favre D, Takeda K. 2009. A single polymorphic amino
1139 acid on Toxoplasma gondii kinase ROP16 determines the direct and strain-specific
1140 activation of Stat3. *J Exp Med* 206:2747-60.

- 1141 12. Saeij JP, Coller S, Boyle JP, Jerome ME, White MW, Boothroyd JC. 2007. Toxoplasma co-
1142 opts host gene expression by injection of a polymorphic kinase homologue. Nature
1143 445:324-7.
- 1144 13. Mercier C, Dubremetz JF, Rauscher B, Lecordier L, Sibley LD, Cesbron-Delauw MF. 2002.
1145 Biogenesis of nanotubular network in Toxoplasma parasitophorous vacuole induced by
1146 parasite proteins. Mol Biol Cell 13:2397-409.
- 1147 14. Sibley LD, Niesman IR, Parmley SF, Cesbron-Delauw MF. 1995. Regulated secretion of
1148 multi-lamellar vesicles leads to formation of a tubulovesicular network in host-cell
1149 vacuoles occupied by *Toxoplasma gondii*. J Cell Sci 108:1669-1677.
- 1150 15. Gold DA, Kaplan AD, Lis A, Bett GC, Rosowski EE, Cirelli KM, Bougdour A, Sidik SM, Beck
1151 JR, Lourido S, Egea PF, Bradley PJ, Hakimi MA, Rasmusson RL, Saeij JP. 2015. The
1152 Toxoplasma Dense Granule Proteins GRA17 and GRA23 Mediate the Movement of Small
1153 Molecules between the Host and the Parasitophorous Vacuole. Cell Host Microbe
1154 17:642-52.
- 1155 16. Pernas L, Adomako-Ankomah Y, Shastri AJ, Ewald SE, Treeck M, Boyle JP, Boothroyd JC.
1156 2014. Toxoplasma effector MAF1 mediates recruitment of host mitochondria and
1157 impacts the host response. PLoS Biol 12:e1001845.
- 1158 17. Cesbron-Delauw MF, Guy B, Torpier G, Pierce RJ, Lenzen G, Cesbron JY, Charif H, Lepage
1159 P, Darcy F, Lecocq JP, et al. 1989. Molecular characterization of a 23-kilodalton major
1160 antigen secreted by *Toxoplasma gondii*. Proc Natl Acad Sci U S A 86:7537-41.
- 1161 18. Gay G, Braun L, Brenier-Pinchart MP, Vollaire J, Josserand V, Bertini RL, Varesano A,
1162 Touquet B, De Bock PJ, Coute Y, Tardieux I, Bougdour A, Hakimi MA. 2016. Toxoplasma

- 1163 gondii TgIST co-opts host chromatin repressors dampening STAT1-dependent gene
1164 regulation and IFN-gamma-mediated host defenses. *J Exp Med* 213:1779-98.
- 1165 19. Bougdour A, Durandau E, Brenier-Pinchart MP, Ortet P, Barakat M, Kieffer S, Curt-
1166 Varesano A, Curt-Bertini RL, Bastien O, Coute Y, Pelloux H, Hakimi MA. 2013. Host cell
1167 subversion by *Toxoplasma* GRA16, an exported dense granule protein that targets the
1168 host cell nucleus and alters gene expression. *Cell Host Microbe* 13:489-500.
- 1169 20. He H, Brenier-Pinchart MP, Braun L, Kraut A, Touquet B, Coute Y, Tardieux I, Hakimi MA,
1170 Bougdour A. 2018. Characterization of a *Toxoplasma* effector uncovers an alternative
1171 GSK3/beta-catenin-regulatory pathway of inflammation. *Elife* 7.
- 1172 21. Braun L, Brenier-Pinchart MP, Yogavel M, Curt-Varesano A, Curt-Bertini RL, Hussain T,
1173 Kieffer-Jaquinod S, Coute Y, Pelloux H, Tardieux I, Sharma A, Belrhali H, Bougdour A,
1174 Hakimi MA. 2013. A *Toxoplasma* dense granule protein, GRA24, modulates the early
1175 immune response to infection by promoting a direct and sustained host p38 MAPK
1176 activation. *J Exp Med* 210:2071-86.
- 1177 22. Braun L, Brenier-Pinchart MP, Hammoudi PM, Cannella D, Kieffer-Jaquinod S, Vollaire J,
1178 Josserand V, Touquet B, Coute Y, Tardieux I, Bougdour A, Hakimi MA. 2019. The
1179 *Toxoplasma* effector TEEGR promotes parasite persistence by modulating NF-kappaB
1180 signalling via EZH2. *Nat Microbiol* doi:10.1038/s41564-019-0431-8.
- 1181 23. Panas MW, Naor A, Cygan AM, Boothroyd JC. 2019. *Toxoplasma* Controls Host Cyclin E
1182 Expression through the Use of a Novel MYR1-Dependent Effector Protein, HCE1. *MBio*
1183 10.

- 1184 24. Nadipuram SM, Kim EW, Vashisht AA, Lin AH, Bell HN, Coppens I, Wohlschlegel JA,
1185 Bradley PJ. 2016. In Vivo Biotinylation of the Toxoplasma Parasitophorous Vacuole
1186 Reveals Novel Dense Granule Proteins Important for Parasite Growth and Pathogenesis.
1187 MBio 7.
- 1188 25. Franco M, Panas MW, Marino ND, Lee MC, Buchholz KR, Kelly FD, Bednarski JJ, Sleckman
1189 BP, Pourmand N, Boothroyd JC. 2016. A Novel Secreted Protein, MYR1, Is Central to
1190 Toxoplasma's Manipulation of Host Cells. MBio 7.
- 1191 26. Marino ND, Panas MW, Franco M, Theisen TC, Naor A, Rastogi S, Buchholz KR, Lorenzi
1192 HA, Boothroyd JC. 2018. Identification of a novel protein complex essential for effector
1193 translocation across the parasitophorous vacuole membrane of *Toxoplasma gondii*. PLoS
1194 Pathog 14:e1006828.
- 1195 27. Cygan AM, Theisen, T. C., Mendoza, A. G., Marino, N. D., Panas, M. W., and Boothroyd, J.
1196 C. 2019. Co-immunoprecipitation with MYR1 identifies three additional proteins within
1197 the *Toxoplasma parasitophorous vacuole* required for translocation of dense granule
1198 effectors into host cells. bioRxiv 867788.
- 1199 28. Hakimi MA, Olias P, Sibley LD. 2017. *Toxoplasma* Effectors Targeting Host Signaling and
1200 Transcription. Clin Microbiol Rev 30:615-645.
- 1201 29. Hirai K, Hirato K, Yanagwa R. 1966. A cinematographic study of the penetration of
1202 cultured cells by *Toxoplasma gondii*. Jpn J Vet Res 14:81-90.
- 1203 30. Kimata I, Tanabe K. 1987. Secretion by *Toxoplasma gondii* of an antigen that appears to
1204 become associated with the parasitophorous vacuole membrane upon invasion of the
1205 host cell. J Cell Sci 88:231-9.

- 1206 31. Naor A, Panas MW, Marino N, Coffey MJ, Tonkin CJ, Boothroyd JC. 2018. MYR1-
1207 Dependent Effectors Are the Major Drivers of a Host Cell's Early Response to
1208 Toxoplasma, Including Counteracting MYR1-Independent Effects. *MBio* 9.
- 1209 32. Koshy AA, Dietrich HK, Christian DA, Melehani JH, Shastri AJ, Hunter CA, Boothroyd JC.
1210 2012. Toxoplasma co-opts host cells it does not invade. *PLoS Pathog* 8:e1002825.
- 1211 33. Luder CG, Walter W, Beuerle B, Maeurer MJ, Gross U. 2001. Toxoplasma gondii down-
1212 regulates MHC class II gene expression and antigen presentation by murine
1213 macrophages via interference with nuclear translocation of STAT1alpha. *Eur J Immunol*
1214 31:1475-84.
- 1215 34. Kim SK, Fouts AE, Boothroyd JC. 2007. Toxoplasma gondii Dysregulates IFN- γ -
1216 Inducible Gene Expression in Human Fibroblasts: Insights from a Genome-Wide
1217 Transcriptional Profiling. *J Immunol* 178:5154-65.
- 1218 35. Dubey JP. 1992. Isolation of Toxoplasma gondii from a naturally infected beef cow. *J*
1219 *Parasitol* 78:151-3.
- 1220 36. Khan A, Behnke MS, Dunay IR, White MW, Sibley LD. 2009. Phenotypic and gene
1221 expression changes among clonal type I strains of Toxoplasma gondii. *Eukaryot Cell*
1222 8:1828-36.
- 1223 37. Ziegenhain C, Vieth B, Parekh S, Reinius B, Guillaumet-Adkins A, Smets M, Leonhardt H,
1224 Heyn H, Hellmann I, Enard W. 2017. Comparative Analysis of Single-Cell RNA Sequencing
1225 Methods. *Mol Cell* 65:631-643 e4.

- 1226 38. Brunet J, Pfaff AW, Abidi A, Unoki M, Nakamura Y, Guinard M, Klein JP, Candolfi E,
1227 Mousli M. 2008. *Toxoplasma gondii* exploits UHRF1 and induces host cell cycle arrest at
1228 G2 to enable its proliferation. *Cell Microbiol* 10:908-20.
- 1229 39. Molestina RE, El-Guendy N, Sinai AP. 2008. Infection with *Toxoplasma gondii* results in
1230 dysregulation of the host cell cycle. *Cell Microbiol* 10:1153-65.
- 1231 40. Sabou M, Doderer-Lang C, Leyer C, Konjic A, Kubina S, Lennon S, Rohr O, Viville S,
1232 Cianferani S, Candolfi E, Pfaff AW, Brunet J. 2019. *Toxoplasma gondii* ROP16 kinase
1233 silences the cyclin B1 gene promoter by hijacking host cell UHRF1-dependent epigenetic
1234 pathways. *Cell Mol Life Sci* doi:10.1007/s00018-019-03267-2.
- 1235 41. Velasquez ZD, Conejeros I, Larrazabal C, Kerner K, Hermosilla C, Taubert A. 2019.
1236 *Toxoplasma gondii*-induced host cellular cell cycle dysregulation is linked to
1237 chromosome missegregation and cytokinesis failure in primary endothelial host cells. *Sci*
1238 *Rep* 9:12496.
- 1239 42. Pinney DF, Emerson CP, Jr. 1989. 10T1/2 cells: an in vitro model for molecular genetic
1240 analysis of mesodermal determination and differentiation. *Environ Health Perspect*
1241 80:221-7.
- 1242 43. Subramanian A, Tamayo P, Mootha VK, Mukherjee S, Ebert BL, Gillette MA, Paulovich A,
1243 Pomeroy SL, Golub TR, Lander ES, Mesirov JP. 2005. Gene set enrichment analysis: a
1244 knowledge-based approach for interpreting genome-wide expression profiles. *Proc Natl*
1245 *Acad Sci U S A* 102:15545-50.

- 1246 44. Chen L, Christian DA, Kochanowsky JA, Phan AT, Clark JT, Wang S, Berry C, Oh J, Chen X,
1247 Roos DS, Beiting DP, Koshy AA, Hunter CA. 2020. The *Toxoplasma gondii* virulence factor
1248 ROP16 acts in cis and trans, and suppresses T cell responses. *J Exp Med* 217.
- 1249 45. Park E, Patel S, Wang Q, Andhey P, Zaitsev K, Porter S, Hershey M, Bern M, Plougastel-
1250 Douglas B, Collins P, Colonna M, Murphy KM, Oltz E, Artyomov M, Sibley LD, Yokoyama
1251 WM. 2019. *Toxoplasma gondii* infection drives conversion of NK cells into ILC1-like cells.
1252 *Elife* 8.
- 1253 46. Young J, Dominicus C, Wagener J, Butterworth S, Ye X, Kelly G, Ordan M, Saunders B,
1254 Instrell R, Howell M, Stewart A, Treeck M. 2019. A CRISPR platform for targeted in vivo
1255 screens identifies *Toxoplasma gondii* virulence factors in mice. *Nat Commun* 10:3963.
- 1256 47. Poupel O, Boleti H, Axisa S, Couture-Tosi E, Tardieux I. 2000. Toxofilin, a novel actin-
1257 binding protein from *Toxoplasma gondii*, sequesters actin monomers and caps actin
1258 filaments. *Mol Biol Cell* 11:355-68.
- 1259 48. Sinai AP, Joiner KA. 2001. The *Toxoplasma gondii* protein ROP2 mediates host organelle
1260 association with the parasitophorous vacuole membrane. *J Cell Biol* 154:95-108.
- 1261 49. Reese ML, Boothroyd JC. 2009. A helical membrane-binding domain targets the
1262 *Toxoplasma* ROP2 family to the parasitophorous vacuole. *Traffic* 10:1458-70.
- 1263 50. Carey KL, Jongco AM, Kim K, Ward GE. 2004. The *Toxoplasma gondii* rhoptry protein
1264 ROP4 is secreted into the parasitophorous vacuole and becomes phosphorylated in
1265 infected cells. *Eukaryot Cell* 3:1320-30.

- 1266 51. Hajj HE, Lebrun M, Fourmaux MN, Vial H, Dubremetz JF. 2006. Characterization,
1267 biosynthesis and fate of ROP7, a ROP2 related rhoptry protein of *Toxoplasma gondii*.
1268 *Mol Biochem Parasitol* 146:98-100.
- 1269 52. Wei F, Wang W, Liu Q. 2013. Protein kinases of *Toxoplasma gondii*: functions and drug
1270 targets. *Parasitol Res* 112:2121-9.
- 1271 53. Werk R. 1985. How does *Toxoplasma gondii* enter host cells? *Rev Infect Dis* 7:449-57.
- 1272 54. Dubey JP. 2010. *Toxoplasma gondii* infections in chickens (*Gallus domesticus*):
1273 prevalence, clinical disease, diagnosis and public health significance. *Zoonoses Public*
1274 *Health* 57:60-73.
- 1275 55. Kim SG, Seo SH, Shin JH, Yang JP, Lee SH, Shin EH. 2019. Increase in the nuclear
1276 localization of PTEN by the *Toxoplasma* GRA16 protein and subsequent induction of
1277 p53-dependent apoptosis and anticancer effect. *J Cell Mol Med*
1278 doi:10.1111/jcmm.14207.
- 1279 56. Shen B, Brown KM, Lee TD, Sibley LD. 2014. Efficient gene disruption in diverse strains of
1280 *Toxoplasma gondii* using CRISPR/CAS9. *MBio* 5:e01114-14.
- 1281 57. van Dooren GG, Tomova C, Agrawal S, Humbel BM, Striepen B. 2008. *Toxoplasma gondii*
1282 Tic20 is essential for apicoplast protein import. *Proc Natl Acad Sci U S A* 105:13574-9.
- 1283 58. Sadak A, Taghy Z, Fortier B, Dubremetz JF. 1988. Characterization of a family of rhoptry
1284 proteins of *Toxoplasma gondii*. *Mol Biochem Parasitol* 29:203-11.
- 1285 59. Picelli S, Faridani OR, Bjorklund AK, Winberg G, Sagasser S, Sandberg R. 2014. Full-length
1286 RNA-seq from single cells using Smart-seq2. *Nat Protoc* 9:171-81.

- 1287 60. Zehua Liu HL, Kaikun Xie, Hao Wang, Ning Chen, Oscar M. Aparicio, Machael Q. Zhang,
1288 Rui Jiang, Ting Chen. 2017. Reconstructing cell cycle pseudo time-series via single-cell
1289 transcriptome data. *Nature Communications* 8:9.
- 1290 61. Tirosh I, Izar B, Prakadan SM, Wadsworth MH, 2nd, Treacy D, Trombetta JJ, Rotem A,
1291 Rodman C, Lian C, Murphy G, Fallahi-Sichani M, Dutton-Regester K, Lin JR, Cohen O,
1292 Shah P, Lu D, Genshaft AS, Hughes TK, Ziegler CG, Kazer SW, Gaillard A, Kolb KE, Villani
1293 AC, Johannessen CM, Andreev AY, Van Allen EM, Bertagnolli M, Sorger PK, Sullivan RJ,
1294 Flaherty KT, Frederick DT, Jane-Valbuena J, Yoon CH, Rozenblatt-Rosen O, Shalek AK,
1295 Regev A, Garraway LA. 2016. Dissecting the multicellular ecosystem of metastatic
1296 melanoma by single-cell RNA-seq. *Science* 352:189-96.
- 1297 62. Whitfield ML, Sherlock G, Saldanha AJ, Murray JI, Ball CA, Alexander KE, Matese JC,
1298 Perou CM, Hurt MM, Brown PO, Botstein D. 2002. Identification of genes periodically
1299 expressed in the human cell cycle and their expression in tumors. *Mol Biol Cell* 13:1977-
1300 2000.
- 1301 63. Hiyama H, Iavarone A, Reeves SA. 1998. Regulation of the cdk inhibitor p21 gene during
1302 cell cycle progression is under the control of the transcription factor E2F. *Oncogene*
1303 16:1513-23.
- 1304 64. Horne MC, Goolsby GL, Donaldson KL, Tran D, Neubauer M, Wahl AF. 1996. Cyclin G1
1305 and cyclin G2 comprise a new family of cyclins with contrasting tissue-specific and cell
1306 cycle-regulated expression. *J Biol Chem* 271:6050-61.
- 1307 65. Bostrom J, Sramkova Z, Salasova A, Johard H, Mahdessian D, Fedr R, Marks C, Medalova
1308 J, Soucek K, Lundberg E, Linnarsson S, Bryja V, Sekyrova P, Altun M, Andang M. 2017.

- 1309 Comparative cell cycle transcriptomics reveals synchronization of developmental
1310 transcription factor networks in cancer cells. *PLoS One* 12:e0188772.
- 1311 66. Hirose K, Kawashima T, Iwamoto I, Nosaka T, Kitamura T. 2001. MgcRacGAP is involved
1312 in cytokinesis through associating with mitotic spindle and midbody. *J Biol Chem*
1313 276:5821-8.
- 1314 67. Fontijn RD, Goud B, Echard A, Jollivet F, van Marle J, Pannekoek H, Horrevoets AJ. 2001.
1315 The human kinesin-like protein RB6K is under tight cell cycle control and is essential for
1316 cytokinesis. *Mol Cell Biol* 21:2944-55.
- 1317 68. Santos A, Wernersson R, Jensen LJ. 2015. Cyclebase 3.0: a multi-organism database on
1318 cell-cycle regulation and phenotypes. *Nucleic Acids Res* 43:D1140-4.
- 1319 69. Wolf FA, Angerer P, Theis FJ. 2018. SCANPY: large-scale single-cell gene expression data
1320 analysis. *Genome Biol* 19:15.
- 1321 70. Finak G, McDavid A, Yajima M, Deng J, Gersuk V, Shalek AK, Slichter CK, Miller HW,
1322 McElrath MJ, Prlic M, Linsley PS, Gottardo R. 2015. MAST: a flexible statistical
1323 framework for assessing transcriptional changes and characterizing heterogeneity in
1324 single-cell RNA sequencing data. *Genome Biol* 16:278.
- 1325 71. Gennady Korotkevich VS, Alexey Sergushichev. 2019. Fast gene set enrichment analysis.
1326 bioRxiv doi:<https://doi.org/10.1101/060012>

1327

1328

1329 **MAIN TEXT FIGURE AND TABLE LEGENDS**

1330 **Figure 1.** Key experimental conditions and comparisons. **(A)** Simplified illustration of
1331 effector secretion during early tachyzoite infection. Blue curved arrows = modulation of
1332 host transcription, black curved arrows = transitions through stages of lytic cycle, blue
1333 jagged arrow = modulation without translocation to the nucleus, ROPs = rhoptry
1334 proteins, MIGs = MYR-independent dense granule proteins, MDGs = MYR-dependent
1335 dense granule proteins, MYR = putative translocation required for MDG penetration of
1336 host cytosol. **(B)** As a result of the events in (A), infected host cell monolayers produce
1337 infected-injected (I-I) cells when tachyzoite invasion proceeds as usual, uninfected-
1338 uninjected (U-U) bystander cells, and uninfected-injected (U-I) cells from aborted
1339 invasion after effector injection. **(C)** Parasite-dependent stimuli (i.e., effectors, paracrine
1340 factors) that influence each of seven cell species collected for RNA sequencing,
1341 according to the current model of effector secretion for *Toxoplasma* tachyzoites. Wt and
1342 Dmyr1 designate cells originating from host cell monolayers infected with wild type and
1343 Dmyr1 parasites, respectively; Mock indicates cells from a mock-infected monolayer. **(D)**
1344 Parasite-dependent stimuli that explain the differences in expression trends between
1345 key pairs of collected cell species. PV = parasitophorous vacuole.
1346

1347 **Figure 2.** Experimental pipeline. **(A)** Pipeline to collect and analyze experimental
1348 conditions for single cell RNA sequencing. BLA = toxofilin-beta-lactamase ROP fusion
1349 protein, CCF2-AM = indicator dye that reveals injected (blue) vs. uninjected (green)
1350 cells, U-U = uninfected-uninjected bystander host cell, U-I = uninfected-injected host cell,
1351 and I-I = infected-injected host cell. **(B)** FACS gating strategy to obtain mock-infected,
1352 U-U, I-I, and U-I cells. For cells originating from the parasite-free gate, the distribution of

1353 sorted U-I (orange) and U-U (pink) cells from each of the 1 hpi, 2 hpi, and 3 hpi time
1354 points is shown. **(C)** Proportion of injected (U-I + I-I) cells that are U-I. **(D)** Abundances
1355 of U-U, I-I, and U-I cells during FACS, expressed as percentages of cells from the
1356 Live/Mock gate from which they were sorted.

1357

1358 **Figure 3.** Infection response recapitulates previously identified signatures of early
1359 infection. **(A)** Gene set enrichment analysis (GSEA) of the ranked list of differentially
1360 expressed genes between Wt I-I and mock cells at 2 hpi (FDR < 0.1, FC > 1.5x) using
1361 the Hallmark gene sets from the Molecular Signatures Database. **(B)** GSEA as in (A) of
1362 the ranked differentially expressed genes between Wt I-I and mock cells at 3 hpi. FDR =
1363 false discovery rate, NES = normalized enrichment score, and FC = fold change. Gray
1364 cells indicate pathways common to those identified with FDR < 10⁻⁵ in Naor et al. 2018.

1365

1366 **Figure 4.** Host response to injected parasite effectors. **(A)** Gene set enrichment
1367 analysis (GSEA) of the ranked list of differentially expressed genes (DEGs; false
1368 discovery rate (FDR) < 0.1, fold change > 1.5x) between Wt U-I and Wt U-U cells at 3
1369 hpi using the Hallmark gene sets. Green rows indicate gene sets enriched from genes
1370 expressed higher in Wt U-I than in Wt U-U, and red rows indicate gene sets enriched in
1371 genes expressed lower in Wt U-I than in Wt U-U. Gene sets are designated as part of
1372 the infection response if they were also found to be enriched from DEGs between Wt I-I
1373 vs. Mock at 2 hpi or 3 hpi. **(B)** GSEA as in (A) between various U-I cells (i.e., from the
1374 Wt, CytD, and Dmyr1 infection conditions) and their cognate U-U cells at 3 hpi. Gene
1375 sets in bold gray text were also found to be enriched in the infection response. Positive

1376 normalized enrichment scores represent enrichment in genes expressed higher in U-I
1377 cells than in U-U cells.

1378

1379 **Figure 5.** Comparison of host response to injection vs. infection (i.e., signatures in Wt
1380 U-I vs. Wt I-I cells.) **(A)** Scatterplot comparing injection-associated genes in Wt I-I cells
1381 and Wt U-I cells, as determined by the Spearman correlation of gene expression to the
1382 CCF2-AM ratio in Wt I-I and Wt U-I cells. Contours reflect density of points, with central
1383 contours being in the area of highest density. Labeled points on the plot are the top 20
1384 genes with the lowest probability of belonging to a Gaussian model fit with parameters
1385 that best describe the observed Spearman correlation data. Yellow and blue shading
1386 mark regions of the scatterplots where gene expression trends in Wt U-I cells are either
1387 enhanced or dampened upon parasite invasion and release of dense granule effectors
1388 into the host cell (as seen in Wt I-I cells). **(B)** GSEA of the ranked list of differentially
1389 expressed genes between Wt U-I and Wt I-I cells at 3 hpi, where green rows denote
1390 gene sets enriched from genes expressed higher in Wt U-I cells than in Wt I-I cells, and
1391 red rows represent genes expressed higher in Wt I-I than in Wt U-I. FDR = false
1392 discovery rate, NES = normalized enrichment score.

1393

1394 **Figure 6.** GSEA of the ranked list of differentially expressed genes between Dmyr1 U-I
1395 and Dmyr1 I-I cells at 3 hpi, which illustrates the impact of MYR-independent dense
1396 granule proteins (MIGs) and parasite invasion on the host response to infection with
1397 *Toxoplasma*. Green rows denote gene sets enriched from genes expressed higher in
1398 Dmyr1 U-I cells than in Dmyr1 I-I cells, and red rows represent genes expressed higher

1399 in Dmyr1 I-I cells than in Dmyr1 U-I cells. FDR = false discovery rate, NES = normalized
1400 enrichment score.

1401

1402 **Figure 7.** Impact of MYR-dependent dense granule proteins (MDGs) and MYR-
1403 dependent paracrine effectors, as illustrated by comparing Dmyr1 I-I and Wt I-I cells. **(A)**
1404 Gene set enrichment analysis (GSEA) of ranked list of differentially expressed genes
1405 between Dmyr1 I-I and Wt I-I cells at 3 hpi. Green rows denote enrichment from genes
1406 expressed higher in Dmyr1 I-I cells than in Wt I-I cells, and red rows represent
1407 enrichment from genes expressed higher in Wt I-I than in Wt U-I. FDR = false discovery
1408 rate, NES = normalized enrichment score. **(B)** Scatterplot comparing injection-
1409 associated genes in Dmyr1 I-I cells and Wt I-I cells, as determined by the Spearman
1410 correlation of gene expression to the CCF2-AM ratio in Dmyr1 I-I and Wt I-I cells.
1411 Contours reflect density of points, with central contours being in the area of highest
1412 density. Labeled points on the plot are the top 20 genes with the lowest probability of
1413 belonging to a Gaussian model fit with parameters that best describe the observed
1414 Spearman correlation data. Yellow and blue shading mark regions of the scatterplots
1415 where gene expression trends in Dmyr1 I-I cells are either enhanced or dampened by
1416 MDGs or paracrine effects (as seen in Wt I-I cells).

1417

1418 **Figure 8.** Comparison of Dmyr1 U-U vs. Mock cell types reveals impact of MYR-
1419 dependent paracrine effects on host cell transcription during *Toxoplasma* infection. **(A)**
1420 Gene set enrichment analysis (GSEA) of the ranked list of differentially expressed
1421 genes between Dmyr1 U-U and Mock cells at 3 hpi. FDR = false discovery rate, NES =

1422 normalized enrichment score, and sc = the current single cell RNA-seq dataset. **(B)**
1423 Trends in expression of Dmyr1 U-U vs. Mock DEGs are conserved in U-I and I-I cells
1424 from Wt and Dmyr1 infections, as illustrated by strip plots depicting expression of DEGs
1425 between Dmyr1 U-U and Mock cells across all cell types. Each point represents a single
1426 cell, and its y-axis displacement reflects the average of the normalized expression
1427 scores for all DEGs between Dmyr1 U-U and Mock cells. The normalized expression
1428 score of a given gene is calculated by scaling the log₂ count per median (cpm) for that
1429 gene, such that the cell with the lowest cpm receives a score of 0, and the cell with the
1430 highest cpm receives a score of 1.

1431

1432 **Figure 9.** Summary of host transcriptional response to parasite-dependent stimuli. **(A)**
1433 Bubble plot of parasite-dependent host transcriptional signatures at 3 hpi that depicts
1434 the behavior of 11 representative Hallmark gene sets from the Molecular Signatures
1435 Database (columns) across 8 key comparisons between experimental conditions (rows,
1436 indicated on left of each plot) that each encapsulates the impact of certain parasite-
1437 dependent stimuli on the 11 gene sets (indicated on right of each plot). Colors indicate
1438 normalized enrichment scores (NES) from gene set enrichment analysis (GSEA) of
1439 differentially expressed genes (DEGs) between each comparison. FDR = false
1440 discovery rate, where FDR < 0.25 is considered significant (as is standard for GSEA).
1441 Parasite-dependent stimuli include ROPs = rhoptry proteins, MDGs = MYR-dependent
1442 dense granule proteins, MIGs = MYR-independent dense granule proteins, P(MD) =
1443 MYR-dependent paracrine effects, P(MI) = MYR-independent paracrine effects, and All
1444 = ROPs + MDGs + MIGs + Invasion + P(MD) + P(MI). **(B)** Bubble plot as in (A) where

1445 colors indicate \log_2 normalized fold change in expression of DEGs that fall under each
1446 comparison and each gene set. **(C)** Model of individual impacts of parasite-dependent
1447 stimuli on host transcription, which include immune pathways (e.g., TNFA Signaling via
1448 NFKB, IL6 JAK STAT3 Signaling, Inflammatory Response, IL2 STAT5 Signaling,
1449 Interferon Gamma Response, and Allograft Rejection), cellular stress (e.g., Hypoxia,
1450 Apoptosis), and cell proliferation-associated pathways (i.e., KRAS signaling, p53
1451 pathway). Curved lines indicate modulation of host transcription, and jagged lines
1452 indicate modulation without effector translocation to the nucleus.

1453

1454 **SUPPLEMENTARY FILE FIGURE AND TABLE LEGENDS**

1455 **Figure S1.** Construction and validation of RH $\Delta myr1$ mCherry Toxofilin-HA-beta-
1456 lactamase (RH $\Delta myr1$ mCherry Tfn-HA-BLA). **(A)** CRISPR/Cas9 strategy to construct
1457 RH $\Delta myr1$ mCherry Tfn-HA-BLA by disrupting parasite UPRT (blue) in parental strain
1458 RH $\Delta myr1$ mCherry. The parental strain was transfected with plasmid pSAG1::- Cas9-
1459 U6::sgUPRT (pink) and a linear amplicon containing Tfn-HA-BLA (purple) and flanked
1460 with 20 nucleotide homology arms to UPRT (blue). The region of UPRT complementary
1461 to the guide RNA, which also contains the site at which Cas9 cleaves, is in pink. **(B)**
1462 Western blot for the Tfn-HA-BLA construct in RH $\Delta myr1$ mCherry Tfn-HA-BLA. All lanes
1463 were obtained from the same gel. **(C)** Immunofluorescence assay (IFA) for
1464 colocalization of the Tfn-HA-BLA protein product and ROP2/3/4. **(D)** FACS analysis of
1465 10 T1/2 cells infected with parasite-free lysate, RH Tfn-HA-BLA, and RH $\Delta myr1$
1466 mCherry Tfn-HA-BLA. Cleavage of reporter dye CCF2-AM indicates injection of the Tfn-
1467 HA-BLA construct.

1468 **Figure S2.** Human foreskin fibroblast (HFF) feeder cell debris contaminates the
1469 uninfected-injected (U-I) FACS gate. In all panels, a host cell monolayer is treated with
1470 either a parasite-free lysate of HFFs or RH Tfn-HA-BLA parasites syringe released from
1471 HFFs and then incubated with CCF2-AM to reveal (un)injected cells. *Left:* Infection with
1472 RH Tfn-HA-BLA reveals uninjected and injected cell populations. *Middle:* Mock
1473 “infection” with parasite-free lysate reveals HFF feeder cell debris contaminating the
1474 “injected” cell population. *Right:* Infection with parasite-free lysate that was washed to
1475 remove HFF debris reveals a reduction in contamination of the injected population.
1476

1477 **Figure S3. (A)** Serum starvation for 24 h partially inhibits cell division of 10 T1/2 host
1478 cells, reducing the possibility of capturing U-I cells that arise from division of an infected
1479 host cell (U-I_d cells) rather than from an aborted invasion event. Note that the S phase
1480 population in the bottom right panel (serum replete, infected cells) also contains G1
1481 phase cells containing parasites, as parasite nuclear content enhances the propidium
1482 iodide signal in these cells. **(B)** Histogram depicting the number of infected host cells
1483 that divided at various times post-infection, as determined by live video microscopy
1484 footage of 200 serum starved 10 T1/2 cells for which the precise moment of infection
1485 was captured on camera. Of the 200 infected 10 T1/2 cells, 53 divided over a 16 hour
1486 time course, and none divided at earlier than 3.67 hours post-infection.

1487
1488 **Figure S4.** Quality control metrics for single cell RNA sequencing data. **(A)** Comparison
1489 of gene counts (number of genes for which reads from each cell mapped to the
1490 concatenated mouse-*Toxoplasma* genome, y-axis) and read sum (total reads, x-axis)

1491 for all experimental trials. Cells that passed quality control are indicated in color. **(B)**
1492 Percentages of total reads that mapped to open reading frames (ORFs) in the mouse-
1493 *Toxoplasma* concatenated genome. **(C) Top panel:** Linear regression modeling of
1494 measurement accuracy fitted on ERCC spike-ins with abundance above the detection
1495 limit. The text within each subplot denotes the coefficient of determination for the
1496 regression fit. *Bottom panel:* Logistic regression modeling of detection limit based on
1497 ERCC spike-ins. The 50% detection rate is indicated with a black dotted line, and the
1498 text within each subplot indicates the detection limit for each experiment in absolute
1499 molecular counts. **(D)** Linear regression fitted to scatterplot of average gene counts of
1500 differentially expressed genes for single cell RNA sequencing data (x-axis) vs. bulk RNA
1501 sequencing data (y-axis). Each point represents a DEG. Text within each subplot
1502 denotes the coefficient of determination (R^2) for the regression. **(E)** The coefficients of
1503 determination for linear regression lines fit to scatterplots as in (D) for all possible
1504 combinations of single vs. bulk RNA-seq combinations.

1505

1506 **Figure S5.** Single cell resolution enables strategic partitioning of individual cells for
1507 downstream analysis. **(A)** Percentage of reads derived from *Toxoplasma* validates
1508 infection status of individual cells. Cells are scored as uninfected if left of the lower
1509 decision line (bold, dashed), infected if right of the upper decision line (dotted), and
1510 ambiguous if between the decision lines (cross-hatched section). **(B)** Principal
1511 component analysis (PCA) projection of cells based on 175 curated cell cycle markers
1512 and subsequent Leiden clustering enables partitioning of cells by predicted cell cycle
1513 states, G1 (green), S (gold), and G2/M (purple). **(C)** Proportion of cells from each

1514 experimental condition in each cell cycle phase. **(D)** Dimensionality reduction and
1515 projection of single cells using the *Uniform Manifold Approximation and Projection*
1516 (UMAP) algorithm reveals 3 putative cell populations. All panels are reproduced copies
1517 of the same projection, each of which is color coded by specific parameters. *Left:*
1518 Louvain clusters, used to assign the cells to populations 1, 2, and 3; *middle:* cell cycle
1519 phase; *right (3 panels):* experimental trial (1 hpi, 2 hpi, and 3 hpi).

1520

1521 **Figure S6.** Effect of cytochalasin D treatment on the proportion of 10 T1/2 host cells
1522 that are U-I cells. **(A)** U-U and U-I cells that arise from Wt and CytD infections at 2 hpi.
1523 **(B)** U-U and U-I cells that arise from Wt and CytD infections at 3 hpi.

1524

1525 **Table S1:** Mouse genes discarded due to reads from extracellular RH parasites
1526 mapping to these genes in the concatenated mouse-*Toxoplasma* genome.

1527

1528 **Table S2:** Curated list of genes used to assign cell cycle phases to single host cells.

1529

1530 **Table S3:** Differentially expressed genes (DEGs). In all tables, *fdr* = false discovery rate,
1531 and *log2FC* is the \log_2 fold change in expression of DEGs between the indicated
1532 conditions. **(A)** All differentially expressed genes at all time points. **(B)** Wt I-I vs. Mock
1533 Differentially Expressed Genes. **(C)** Wt U-I vs. Wt U-U Differentially Expressed Genes.
1534 **(D)** Dmyr1 U-I vs. Dmyr1 U-U Differentially Expressed Genes. **(E)** CytD U-I vs. CytD U-
1535 U Differentially Expressed Genes. **(F)** Wt U-I vs. Wt I-I Differentially Expressed Genes.
1536 **(G)** Dmyr1 U-I vs. Dmyr1 I-I Differentially Expressed Genes. **(H)** Wt I-I vs. Dmyr1 I-I

1537 Differentially Expressed Genes. **(I)** Wt U-U vs. Mock Differentially Expressed Genes. **(J)**

1538 Dmyr1 U-U vs. Mock Differentially Expressed Genes. For (F) and (G), a gene is

1539 designated as showing evidence of being acted upon by counterbalancing effectors

1540 (indicated in the “Evidence of Effectors in Wt I-I Cells Counteracting Effectors in Wt U-I

1541 Cells?” and “Evidence of Effectors in Dmyr1 I-I Cells Counteracting Effectors in Dmyr1

1542 U-I Cells?” columns, respectively) if it exhibits either: 1) upregulation in one cell type

1543 and downregulation in the other compared to a common Wt U-U standard, or 2) more

1544 upregulation or downregulation in Wt U-I cells compared to the standard than in Wt I-I

1545 cells.

1546

1547 **Table S4:** CCF2-AM correlation data for **(A)** Wt U-I vs. Wt I-I cells and **(B)** Dmyr1 I-I vs.

1548 Wt I-I cells. A gene is designated as showing evidence of being acted upon by

1549 counterbalancing effectors (indicated under the “Evidence of Effector

1550 Counterbalancing?” column) if it exhibits either: 1) negative correlation with CCF2-AM in

1551 one cell type and a positive CCF2-AM correlation in the other cell type, or 2) stronger

1552 positive or negative correlations in Wt U-I cells than in Wt I-I cells.

Figure 1

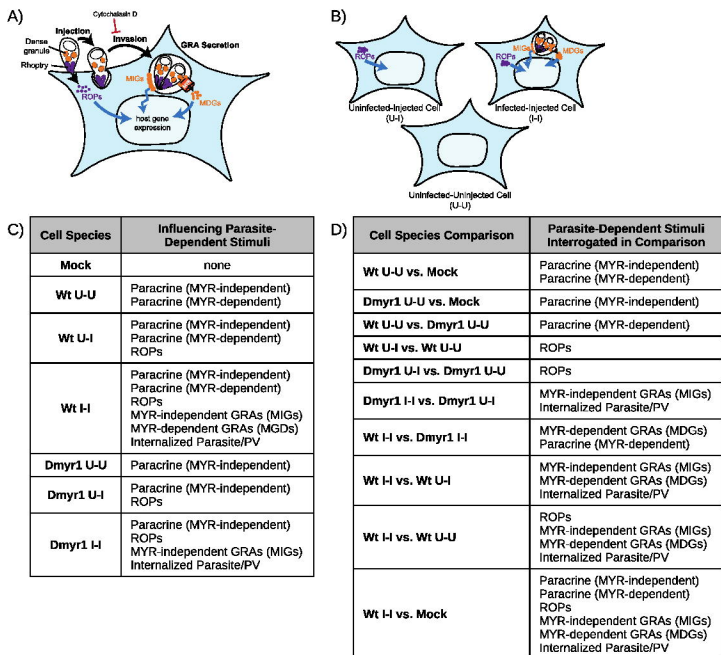


Figure 2

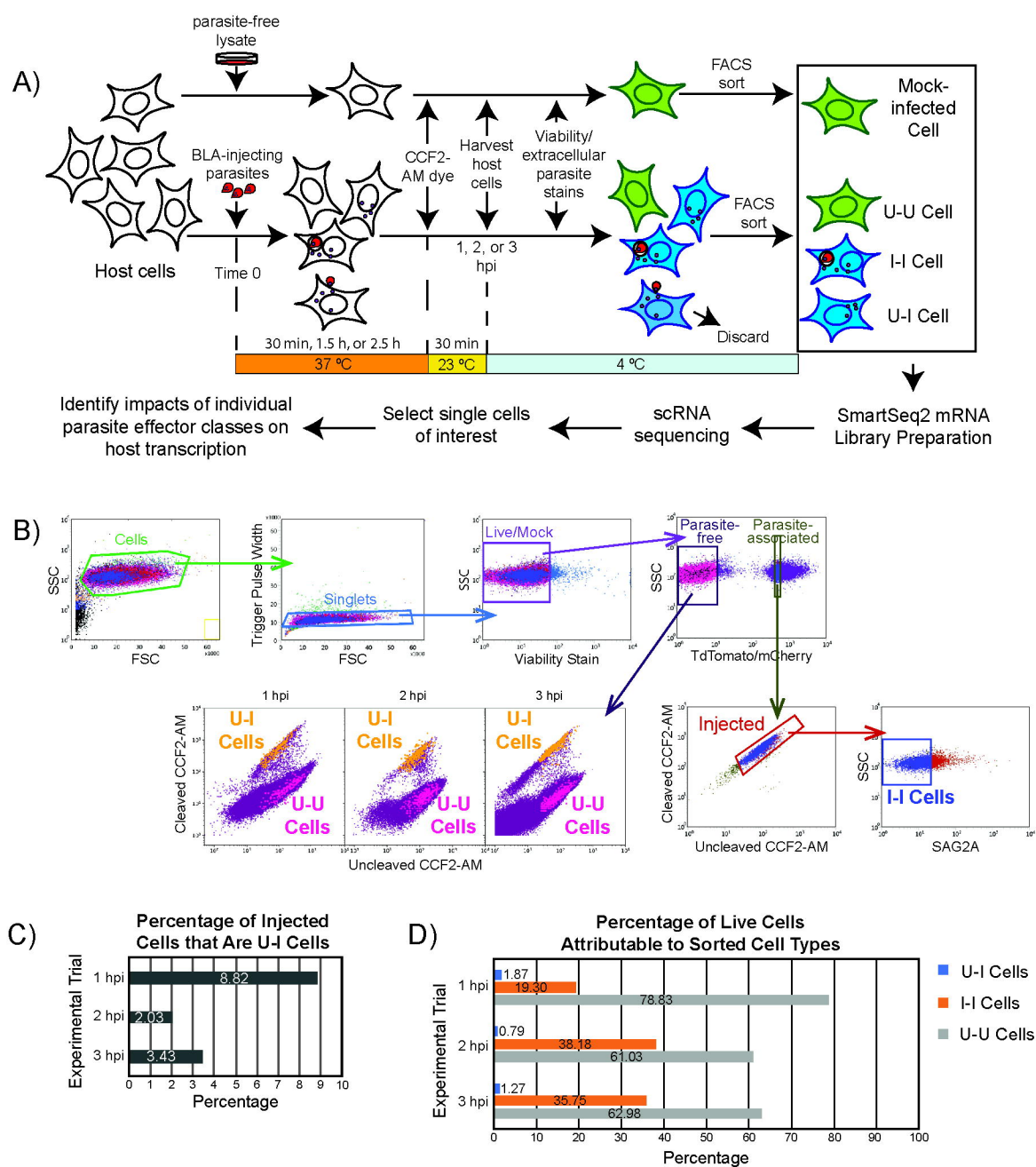


Figure 3

Wt I-I vs mock GSEA (2 hpi)

A)

	Gene Set	FDR	NES	Identified at 6 hpi (Naor et al 2018)
Higher in Wt I-I	TNFA SIGNALING VIA NFKB	0.078	1.888	Yes
	ALLOGRAFT REJECTION	0.086	1.634	Yes
	IL6 JAK STAT3 SIGNALING	0.108	1.692	Yes
	INTERFERON GAMMA RESPONSE	0.108	1.785	Yes
	ESTROGEN RESPONSE LATE	0.169	1.573	Yes
Higher in Mock	TGF BETA SIGNALING	0.199	-1.725	No
	UV RESPONSE DN	0.199	-1.594	Yes

Wt I-I vs mock GSEA (3 hpi)

B)

	Gene Set	FDR	NES	Identified at 6 hpi (Naor et al 2018)
Higher in Wt I-I	TNFA SIGNALING VIA NFKB	0.052	2.596	Yes
	INFLAMMATORY RESPONSE	0.052	2.065	Yes
	ALLOGRAFT REJECTION	0.052	2.062	Yes
	IL6 JAK STAT3 SIGNALING	0.052	1.997	Yes
	APOPTOSIS	0.059	1.85	Yes
	P53 PATHWAY	0.059	1.762	Yes
	IL2 STAT5 SIGNALING	0.071	1.803	Yes
	KRAS SIGNALING DN	0.089	1.703	Yes
	INTERFERON GAMMA RESPONSE	0.103	1.729	Yes
	UV RESPONSE DN	0.148	1.669	Yes
	UV RESPONSE UP	0.159	1.565	Yes
	HEME METABOLISM	0.163	1.574	Yes
	MTORC1 SIGNALING	0.163	1.525	Yes
	MITOTIC SPINDLE	0.185	1.504	No
E2F TARGETS	0.243	1.458	Yes	
Higher in Mock	APICAL SURFACE	0.052	-1.636	No
	OXIDATIVE PHOSPHORYLATION	0.052	-2.191	No
	KRAS SIGNALING UP	0.154	-1.639	No
	COAGULATION	0.159	-1.592	No
	ANGIOGENESIS	0.159	-1.602	No
	MYOGENESIS	0.163	-1.638	Yes

Figure 4

A) GSEA for Wt U-I vs. Wt U-U at 3 hpi

	Gene Set	FDR	NES	Part of Infection Response?
Higher in Wt U-I	TNFA SIGNALING VIA NFKB	0.019	2.699	Yes
	INFLAMMATORY RESPONSE	0.019	2.483	Yes
	KRAS SIGNALING UP	0.019	2.113	No
	IL6 JAK STAT3 SIGNALING	0.019	2.021	Yes
	HYPOXIA	0.058	1.842	No
	IL2 STAT5 SIGNALING	0.06	1.823	Yes
	ALLOGRAFT REJECTION	0.06	1.809	Yes
	EPITHELIAL MESENCHYMAL TRANSITION	0.06	1.787	No
	INTERFERON GAMMA RESPONSE	0.06	1.766	Yes
	P53 PATHWAY	0.064	1.74	Yes
	COMPLEMENT	0.142	1.578	No
	KRAS SIGNALING DN	0.121	1.541	Yes
	APICAL JUNCTION	0.159	1.524	No
	UV RESPONSE DN	0.192	1.491	Yes
	OXIDATIVE PHOSPHORYLATION	0.075	-1.771	Yes
Higher in Wt U-U	NOTCH SIGNALING	0.115	-1.323	No
	UNFOLDED PROTEIN RESPONSE	0.216	-1.416	No
	OXIDATIVE PHOSPHORYLATION	0.075	-1.771	Yes

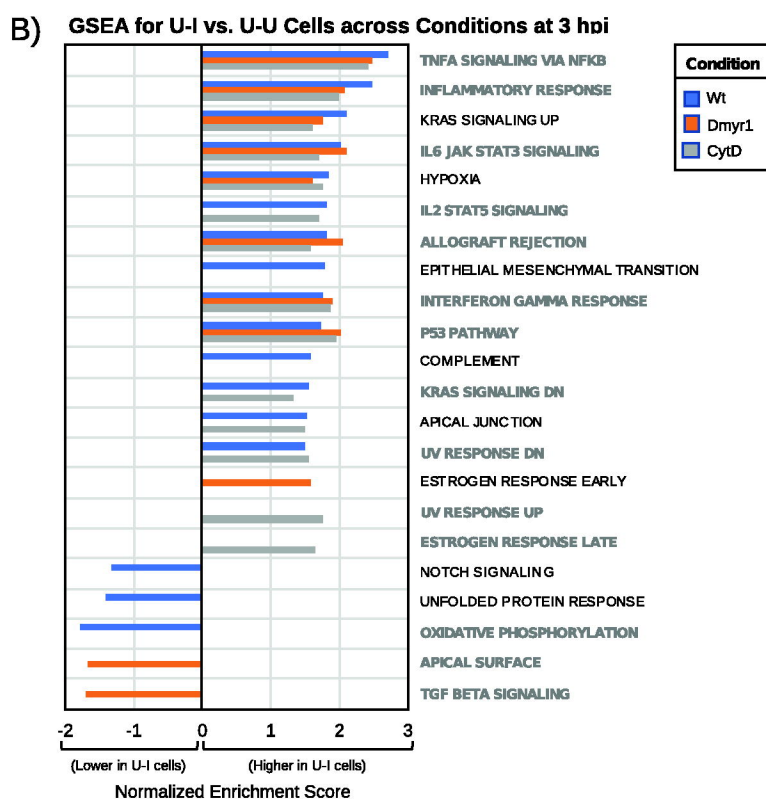


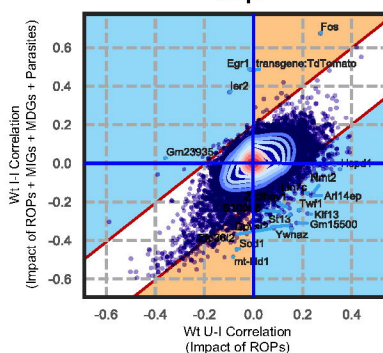
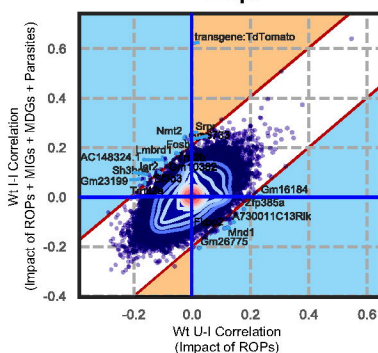
Figure 5

A)

Wt I-I vs Wt U-I CCF2-AM Correlation Plots

2 hpi

3 hpi



■ Impact of ROPs (in Wt U-I cells) *enhanced* by MIGs + MDGs + Parasites (in Wt I-I cells)
■ Impact of ROPs (in Wt U-I cells) *dampened* by MIGs + MDGs + Parasites (in Wt I-I cells)

B)

GSEA for Wt U-I vs. Wt I-I at 3 hpi

	Gene Set	FDR	NES
Higher in Wt U-I	EPITHELIAL MESENCHYMAL TRANSITION	0.050	2.029
	MYOGENESIS	0.050	1.893
	COMPLEMENT	0.054	1.854
	COAGULATION	0.092	1.736
	PI3K AKT MTOR SIGNALING	0.100	1.645
	BILE ACID METABOLISM	0.100	1.574
	XENOBIOTIC METABOLISM	0.198	1.505
	ANDROGEN RESPONSE	0.198	1.487
	KRAS SIGNALING DN	0.198	1.407
	ANGIOGENESIS	0.232	1.334
Higher in Wt I-I	UV RESPONSE UP	0.05	-2.165
	TNFA SIGNALING VIA NFKB	0.081	-1.855
	IL6 JAK STAT3 SIGNALING	0.092	-1.934
	ALLOGRAFT REJECTION	0.100	-1.847
	ESTROGEN RESPONSE EARLY	0.186	-1.593
	INTERFERON GAMMA RESPONSE	0.186	-1.627
	ESTROGEN RESPONSE LATE	0.186	-1.636
	MITOTIC SPINDLE	0.232	-1.458

Figure 6

GSEA for Dmyr1 U-I vs. Dmyr1 I-I at 3 hpi

	Gene Set	FDR	NES	Part of Infection Response?	Part of Injection Response?	Differentially Regulated between Wt I-I and Wt U-I?
Higher in Dmyr1 U-I	COMPLEMENT	0.203	1.427	No	No	Yes
	COAGULATION	0.203	1.427	Yes	No	Yes
	MTORC1 SIGNALING	0.214	1.542	No	No	No
	MYOGENESIS	0.217	1.404	Yes	No	Yes
Higher in Dmyr1 I-I	IL6 JAK STAT3 SIGNALING	0.093	-1.900	Yes	Yes	Yes
	ALLOGRAFT REJECTION	0.126	-1.780	Yes	Yes	Yes
	UV RESPONSE UP	0.126	-1.806	Yes	No	Yes
	INTERFERON GAMMA RESPONSE	0.135	-1.711	Yes	Yes	Yes
	INFLAMMATORY RESPONSE	0.135	-1.738	Yes	Yes	No
	UV RESPONSE DN	0.135	-1.770	Yes	Yes	No
	TNFA SIGNALING VIA NFKB	0.135	-1.830	Yes	Yes	Yes
	P53 PATHWAY	0.189	-1.626	Yes	Yes	No
	KRAS SIGNALING DN	0.203	-1.335	Yes	Yes	No
	ESTROGEN RESPONSE EARLY	0.221	-1.497	No	Yes?	Yes
	ANGIOGENESIS	0.242	-1.312	No	No	No

Figure 7

GSEA for Dmyr1 I-I vs. Wt I-I at 3 hpi

A)

	Gene Set	FDR	NES	Identified at 6 hpi (Naor et al. 2018)	Part of Infection Response	Part of Injection Response
Higher in Dmyr1 I-I	KRAS SIGNALING UP	0.079	2.223	No	No	Yes
	IL2 STAT5 SIGNALING	0.080	2.000	Yes	Yes	Yes
	TNFA SIGNALING VIA NFKB	0.080	1.917	Yes	Yes	Yes
	INFLAMMATORY RESPONSE	0.080	1.891	Yes	Yes	Yes
	ANGIOGENESIS	0.080	1.852	No	No	No
	PI3K AKT MTOR SIGNALING	0.080	1.826	No	No	No
	INTERFERON GAMMA RESPONSE	0.080	1.821	Yes	Yes	Yes
	APOPTOSIS	0.119	1.710	Yes	Yes	No
	IL6 JAK STAT3 SIGNALING	0.083	1.706	Yes	Yes	Yes
	COMPLEMENT	0.153	1.589	No	No	Yes
	GLYCOLYSIS	0.169	1.563	No	No	No
	HYPOXIA	0.153	1.517	Yes	No	Yes
	WNT BETA CATENIN SIGNALING	0.080	1.516	No	No	No
	HEDGEHOG SIGNALING	0.169	1.511	No	No	No
	NOTCH SIGNALING	0.169	1.504	No	No	No
Higher in Wt I-I	MITOTIC SPINDLE	0.124	-1.635	Yes	No	No

B)

Dmyr1 I-I vs Wt I-I CCF2-AM Correlation Plots

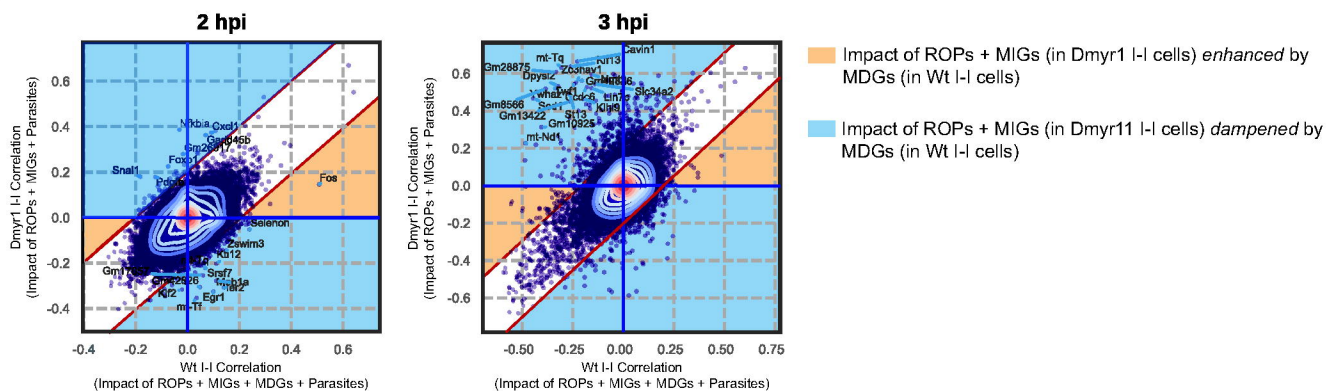


Figure 8

A) GSEA for Dmyr1 U-U vs. Mock at 3 hpi

	Gene Set	FDR	NES	Part of Infection Response (sc)	Part of Infection Response (Naor et al. 2018)	Part of Infection Response (sc)
Higher in Dmyr1 U-U than in Mock	TNFA SIGNALING VIA NFKB	0.012	2.557	Yes	Yes	Yes
	HYPOXIA	0.012	2.000	No	Yes	Yes
	IL6 JAK STAT3 SIGNALING	0.012	2.070	Yes	Yes	Yes
	INFLAMMATORY RESPONSE	0.012	2.304	Yes	Yes	Yes
	P53 PATHWAY	0.012	2.100	Yes	Yes	Yes
	KRAS SIGNALING UP	0.012	2.143	Yes (downregulated)	Yes	Yes
	CHOLESTEROL HOMEOSTASIS	0.026	1.834	No	Yes	No
	ALLOGRAFT REJECTION	0.026	1.783	Yes	Yes	Yes
	APOPTOSIS	0.029	1.790	Yes	Yes	No
	MTORC1 SIGNALING	0.029	1.741	Yes	Yes	No
	INTERFERON GAMMA RESPONSE	0.044	1.733	Yes	Yes	Yes
	XENOBIOTIC METABOLISM	0.046	1.725	No	Yes	No
	UV RESPONSE DN	0.046	1.682	Yes	Yes	Yes
	IL2 STATS SIGNALING	0.104	1.617	Yes	Yes	Yes
	GLYCOLYSIS	0.133	1.540	No	Yes	No
	ESTROGEN RESPONSE EARLY	0.164	1.487	No	Yes	No
	MYC TARGETS V2	0.164	1.533	No	Yes	No
	MYOGENESIS	0.162	1.483	Yes (downregulated)	Yes	No
P3K AKT MTOR SIGNALING	0.199	1.444	No	No	No	
UV RESPONSE UP	0.247	1.418	Yes	Yes	Yes	

B) Expression of Dmyr1 U-U vs. Mock DEGs across All Cells

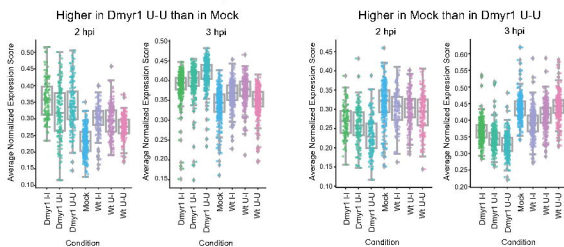
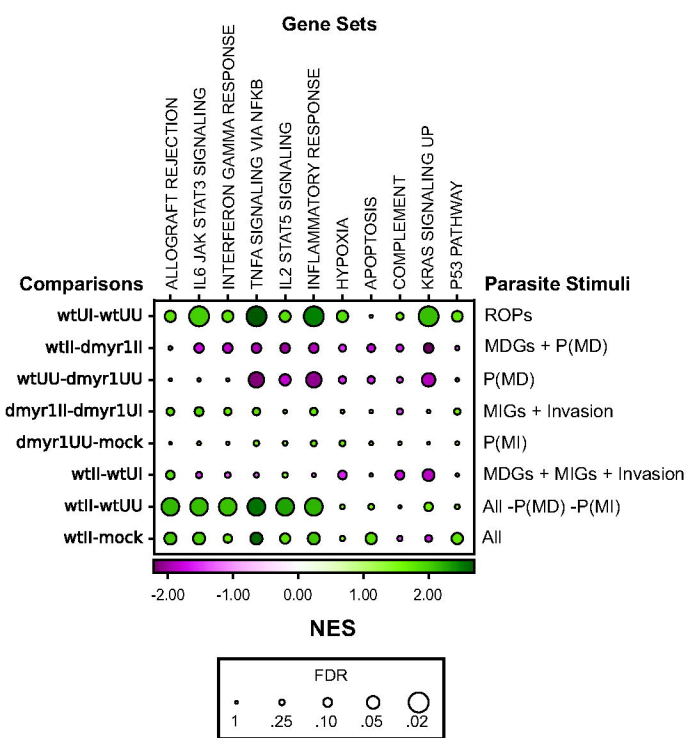
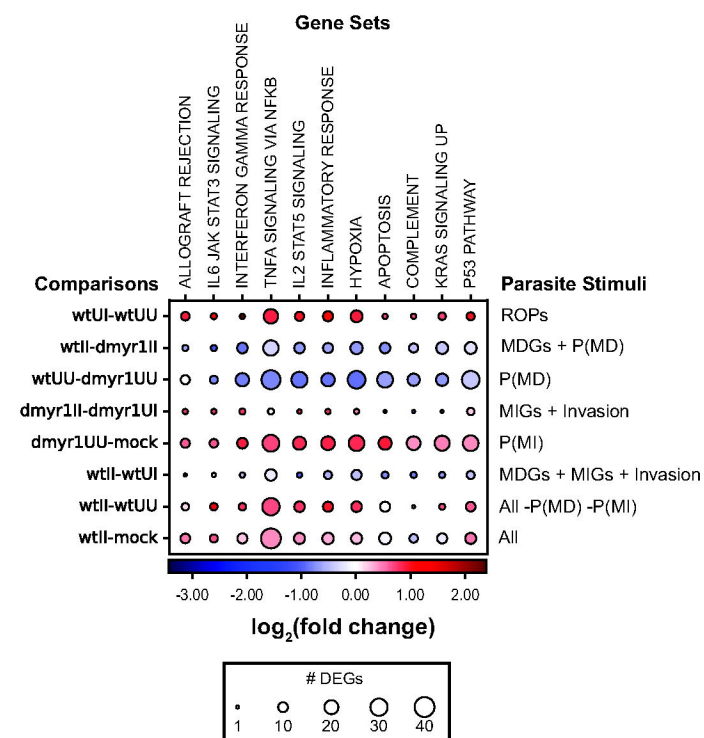


Figure 9

A)



B)



C)

